2015

Tracking Control for Non-Minimum Phase System and Brain Computer Interface

Yacine Boudria
University of Rhode Island, yaciboud@gmail.com

TRACKING CONTROL FOR NON-MINIMUM PHASE SYSTEM AND BRAIN COMPUTER INTERFACE

BY

YACINE BOUDRIA

A DISSERTATION SUBMITTED IN PARTIAL FULFILLMENT OF THE

REQUIREMENTS FOR THE DEGREE OF

DOCTOR OF PHILOSOPHY

IN

ELECTRICALCAL ENGINEERING

UNIVERSITY OF RHODE ISLAND

2015

DOCTOR OF PHILOSOPHY DISSERTATION

OF

YACINE BOUDRIA

APPROVED:

Thesis Committee:

Major Professor Walter Besio

Musa Jouaneh

Richard J. Vaccaro

Leslie A. Mahler

Nasser H. Zawia
DEAN OF THE GRADUATE SCHOOL

UNIVERSITY OF RHODE ISLAND
2015

ABSTRACT

For generations, humans dreamed about the ability to communicate and interact with machines through thought alone or to create devices that can peer into a person's mind and thoughts. Researchers have developed new technologies to create brain computer interfaces (BCIs), communication systems that do not depend on the brain's normal output pathways of peripheral nerves and muscles. The objective of the first part of this thesis is to develop a new BCI based on electroencephalography (EEG) to move a computer cursor over a short training period in real time. The work motivations of this part are to increase: speed and accuracy, as in BCI settings, subject has a few seconds to make a selection with a relatively high accuracy.

Recently, improvements have been developed to make EEG more accurate by increasing the spatial resolution. One such improvement is the application of the surface Laplacian to the EEG, the second spatial derivative. Tripolar concentric ring electrodes (TCREs) automatically perform the Laplacian on the surface potentials and provide better spatial selectivity and signal-to-noise ratio than conventional EEG that is recorded with conventional disc electrodes. Another important feature using TCRE is the capability to record the EEG and the TCRE EEG (tEEG) signals concurrently from the same location on the scalp for the same electrical activity coming from the brain. In this part we also demonstrate that tEEG signals can enable users to control a computer cursor rapidly in different directions with significantly higher accuracy during their first session of training for 1D and 2D cursor control.

Output tracking control of non-minimum phase systems is a highly challenging problem encountered in many practical engineering applications. Classical inversion

techniques provide exact output tracking but lead to internal instability, whereas modern inversion methods provide stable asymptotic tracking but produce large transient errors. Both methods provide an approximation of feedback control, which leads to non robust systems, very sensitive to noise, considerable tracking errors and a significant singularity problem. Aiming at the problem of system inversion to the true system, the objective of the second part of this thesis is to develop a new method based on true inversion for minimum phase system and approximate inversion for non-minimum phase systems. The proposed algorithm is automatic and has minimal computational complexities which make it suitable for real-time control.

The process to develop the proposed algorithm is partitioned into (1) minimum phase feedforward inverse filter, and (2) non-minimum phase inversion. In a minimum phase inversion, we consider the design of a feedforward controller to invert the response of a feedback loop that has stable zero locations. The complete control system consists of a feedforward controller cascaded with a closed-loop system. The outputs of the resulting inverse filter are delayed versions of the corresponding reference input signals, and delays are given by the vector relative degree of the closed-loop.

ACKNOWLEDGMENTS

At first, I owe my deepest gratitude to my advisor, Dr. Walter Besio, to Dr. Richard J. Vaccaro and Dr. Musa Jouaneh, whose guidance, continuous support and motivation enabled me to finish my research.

I am also thankful to Dr. Leslie A. Mahler for her time in participating in my comprehensive exam and dissertation defense.

I am indebted to Dr. G. Faye Boudreaux-Bartels, for her support, guidance and for her valuable suggestions on my work. It really helped me a lot to improve my work.

I would like to thank Rand Kasim Almajidy for helping me recording the 2D data.

I would like to express my appreciation to my parents Seddick Boudria and Ourida Kaoula.

I would like also to express my love and gratitude for my wife, Amal. Her trust in me made me confident enough to accomplish this work. She always is my strongest backup.

PREFACE

This dissertation is written in the manuscript format. It consists of five manuscript organized as follows:

Manuscript 1:

Makeyev, Oleksandr, Yacine Boudria, Zhenghan Zhu, Thomas Lennon, and Walter G. Besio. "Emulating conventional disc electrode with the outer ring of the tripolar concentric ring electrode in phantom and human electroencephalogram data." In *IEEE Signal Processing in Medicine and Biology Symposium, New York City, December*, vol. 7, 4 pp, 2013.

Manuscript 2:

Yacine Boudria, Amal Feltane, and Walter Besio. "Significant improvement in one-dimensional cursor control using Laplacian electroencephalography over electroencephalography." *Journal of Neural Engineering,* vol. 11, 2014.

Manuscript 3:

Yacine Boudria, Rand K. Almajidy, Amal Feltane, Richard J. Vaccaro, Kunal Mankodiya, Ulrich G. Hofmann, Walter G. Besio, “Imagery Tasks Classification using Laplacian EEG and NIRS based BCI ”, *Processed to be submitted to the Journal of Neural Engineering*.

Manuscript 4:

Yacine Boudria, Richard J. Vaccaro, Musa K. Jouaneh, “Phase Compensation of Tracking Control Using Delays of Feedback System”, *The Mediterranean Journal of Measurement and Contro*l, vol. 10, no. 2, pp. 235-243, 2014.

Manuscript 5:

Richard J. Vaccaro, Yacine Boudria, , Musa K. Jouaneh, “Inversion of MIMO Control Systems for Precision Tracking”, *Processed to be submitted to the American Control Conference*.

TABLE OF CONTENTS

LIST OF TABLES

LIST OF FIGURES

INTRODUCTION

Brain activity produces electrical signals that can be detected from the scalp, from the cortical surface, or within the brain [1]. Brain–computer interfaces (BCIs) use these signals to communicate between the brain and the outside world. BCIs enable users to control devices with direct brain communication using electroencephalographic (EEG) activity recorded from electrodes placed on the scalp (noninvasive BCI) [1, 2] or with activity recorded from on or within the brain (invasive BCI) [3, 4]. The EEG is used to monitor brain electrical activity; however EEG signals have low signal to noise ratio (SNR), low spatial resolution, and are contaminated by various artifacts from other sources. These characteristics limit measuring the spatial distribution of brain electrical activity and thus necessitate significant preprocessing [1]. Recently, improvements have been developed to make EEG more accurate by increasing the spatial resolution. One such improvement is the application of the surface Laplacian to the EEG, the second spatial derivative. Tripolar concentric ring electrodes (TCREs) [6, 7] automatically perform the Laplacian on the surface potentials. Previously we have shown that TCRE (Laplacian EEG or tEEG) has significantly better spatial selectivity, SNR, localization, approximation of the analytical Laplacian, and mutual information than conventional EEG with disc electrodes [6, 7]. In manuscript 1, the signal from the outer ring of the TCRE was used as an emulation (eEEG) of EEG recorded using conventional disc electrodes. This allows to record EEG emulation from the exact same locations at the exact same time

as the tEEG using a single recording system. Time domain neuronal signal synchrony was measured using cross-correlation suggesting the potential of eEEG as an emulation of EEG ($r \geq 0.99$).

An important concern in BCI research is to control the computer cursor. Cursor control requires the subject to learn how to adapt their brain signals by using different thought for different tasks [8]. Studies in recent years have shown that EEG-based BCI has great potential in achieving one-dimension cursor control [9-11]. However, these systems usually require long-term training in regulating brain signals and the performance in long-term use is often not robust [12]. For example, Wolpaw *et al* [1] performed over twenty sessions per subject, at a rate of two to four per week to develop high-accuracy cursor control (i.e., >90%) [1]. Slow training of subjects and low spatio-temporal resolution is still a serious problem [8]. In order to make future BCI convenient, the training time must be reduced without loss of accuracy. The objective of manuscript 2 was to compare the accuracy of online 1-Dimensional (1-D) (left-right) computer cursor control using two different types of electrodes, the traditional disc electrode (EEG) and a new tripolar concentric ring electrode (tEEG) [6, 7].

Compared with 1-D cursor control, multidimensional cursor control, such as 2-Dimensional (2-D), provides a much wider range of applications. Most of the multidimensional cursor controls BCIs have been invasive [13]. On the other hand, the development of noninvasive EEG-based 2-D control BCI is delayed by the problem of noisy EEG and the time consumed for subject training. In manuscript 3 we conduct a

2-D (left, right, up and down) computer cursor control using the tEEG signal recorded from subjects performing just one training session.

Although noninvasive EEG-based BCI have been studied increasingly over the recent decades, their performance is still limited. Thus, improving EEG-based BCI performance is still a challenge and the search for paradigms that can detect BCI commands with high temporal resolution is still active. Another noninvasive signal used in the area of BCI is called near infrared spectroscopy (NIRS) [5]. NIRS measures the concentration changes of oxygenated hemoglobins (HbO) and deoxygenated hemoglobins (HbR) in the superficial layers of the human cortex by means of distinct absorption spectra in the near-infrared range [5]. The advantages of NIRS are that it is impervious to the widely-spread environmental electrical noise and much less sensitive to EMG (muscle) artifacts than EEG [5]. NIRS measures oxygenated hemoglobin (Hb) and deoxygenated Hb concentrations. Blood Hb concentration changes have been clearly shown to be related to the presence and absence of the stimulation [5].

The feasibility of using EEG-based motor imagery BCI and NIRS-based motor imagery BCI has been demonstrated in different studies. For example, in [14] they tried to detect motor imagery with online feedback in a NIRS-based motor imagery BCI system. Study [15] introduced a multimodal NIRS and EEG-based system and used NIRS as a predictor for EEG-based BCI performance. In studies [16] and [17], the process was based on the EEG signal to classify the motor imagery based BCI. In manuscript 3, the subjects were asked to use their motor imagery to think about moving their left hands, right hands, both feet or both hands during the appearance of

an arrow to the left, right, up, or down on the computer screen. The mean and the median of the recorded data were used as features to classify the recorded data from tEEG and NIRS into different tasks (left, right, up or down). Two different classifiers were used; the support vector machine (SVM) [18] and the k-nearest neighbor (kNN) [19].

This research also considers the design of digital tracking control systems for minimum phase and non-minimum phase feedback control loops. For a minimum phase system the zeros of the closed-loop system are located inside the unit circle. In the other hand, a non-minimum phase system zeros are locate outside the unit circle.

The complete control system consists of closed-loop control system cascaded with a feedforward inverse system called (FIF). The outputs are delayed versions of the corresponding reference input signals as discussed in manuscript 4. By accounting for delays, theoretically perfect tracking is achieved for minimum phase system. Note that the resulting delay is the relative degree of the closed-loop [20-22]. However, the total delay for a non-minimum phase system is a very challenging process due to the zero locations (zeros outside the unit circle), which require a number of delays larger than the relative degree to do approximate inversion. First, we calculate an exact inverse of the closed-loop system. At this point, the inverse calculated is not stable because the zeros located outside the unit circle becomes poles. Second, we approximate the inverse system by adding more delays until we reach stability. The total delay is the sum of the relative degree with the delay added to reach stability.

Manuscript 5 discussed the tracking control of a fully-coupled Multi-Input Multi-Output (MIMO) plant. We assumed that a 2-degree-of-freedom feedback control

system has been designed to get a stable closed-loop system having zero steady-state error to step inputs. Such a system has an inner feedback loop that stabilizes the plant. In order to have precision tracking for other types of inputs, some type of feedforward control is needed. The main contribution of this manuscript is an algorithm for calculating an inverse filter for the stabilized plant, which is an exact or approximate inverse for the closed-loop system. If the closed-loop system is minimum phase, the result is a decoupled system of delays. If the closed-loop system is non-minimum phase, the result is approximately a decoupled system of delays over a certain bandwidth. The calculation of the inverse filter and resulting tracking performance is demonstrated on an experimental belt-driven H-frame XY table, for which the system to be inverted is fully coupled and non-minimum phase.

The most important advantage of EEG signal over other types of control systems, such as body-powered mechanical systems, is its hands-free control a user's intention. Many real-world applications operated through EEG have been reported, including intelligent wheelchairs, video games, grasping control, television, robotic arm, virtual keyboards, or a neuro-prosthesis that enables the multidimensional movements of a paralyzed limb, etc. [23, 24]. In our future work we will develop an EEG control system to move and control a robotic arm using different mental (motor imagery) commands such as: Forward, Backward, Left, and Right. In general, the proposed EEG control systems to move the robot arm would depend on the subject's mental imagery and can be divided into four stages, namely (1) data acquisition and preprocessing, (2) feature extraction, (3) classification and (4) controller. First, the EEG signal is recorded using a set of electrodes placed on the scalp. Once the data are

recorded, they are preprocessed and then the main characteristics of the recorded data called features will be extracted. In the preprocessing step, the signals will be segmented and filtered to reduce the noise artifacts. This step is important in order to enhance the relevant information embedded in the signals and improving signal quality without losing information. In the second stage, i.e. feature extraction stage, the raw signal obtained from the previous stage is converted into a feature vector. Feature extraction aims at describing the signals with a few relevant values called "features". The third stage is classification, in which categories are identified from the feature vector by employing pattern recognition techniques. This step can also be denoted as feature translation or translation algorithm. Finally, in the fourth stage, i.e. the controller, the categories obtained from the classification stage are translated into control commands to move the robot arm.

References

[1] J. R. Wolpaw and D. J. McFarland, "Control of a two-dimensional movement signal by a noninvasive brain-computer interface in humans," *Proceedings of the National Academy of Sciences of the United States of America*, vol. 101, pp. 17849-17854, 2004.

[2] J. J. Vidal, "Real-time detection of brain events in EEG," *Proceedings of the IEEE,* (special issue on biological signal processing and analysis), vol. 65, pp. 633–664, 1997.

[3] T. N. Lal, T. Hinterberger, G. Widman, M. Schrioder, N. J. Hill, W. Rosenstiel, C. E. Elger, K. Sch¨olkopf and N. Birbaumer, "Methods towards invasive human brain–computer interfaces," *Advances in Neural Information Processing Systems,* (Cambridge, MA: MIT Press), vol. 17, pp. 737–744, 2004.

[4] E. C. Leuthardt, G. Schal, J. R. Wolpaw, J. G. Ojemann and D. Moran, "A brain–computer interface using electrocorticographic signals in humans," *Journal of Neural Engineering,* vol. 1, pp. 63–71, 2004.

[5] Y. Tomita, F. B. Vialatte, G. Dreyfus, Y. Mitsukura, H. Bakardjian and A. Cichocki, "Bimodal BCI using simultaneously NIRS and EEG," *IEEE Transactions on Biomedical Engineering,* , vol. 61, pp. 1274-1284, 2014.

[6] K. Koka, W. Besio, "Improvement of spatial selectivity and decrease of mutual information of tri-polar concentric ring electrodes" *Journal of Neuroscience Methods*, vol. 165, pp. 216-222, 2007.

[7] W. Besio, K. Koka, R. Aakula, and W. Dai, "Tri-polar Concentric Ring Electrode Development for Laplacian Electroencephalography," *IEEE Transactions on Biomedical Engineering*, BME, vol. 53, no. 5, pp. 926-933, 2006.

[8] A. Kostov and M. Polak, "Parallel man-machine training in development of EEG based cursor control," *IEEE Transaction on Rehabilitation Engineering,* vol. 8, pp. 203–4, 2000.

[9] M. Cheng, W. Y. Jia, X. R. Gao,S. K. Gao and F. S. Yang, "Mu-rhythm-based cursor control: an offline analysis," *Clinical Neurophysiology,* vol. 115, pp. 745–51, 2004.

[10] G. E. Fabiani, D. J. McFarland, J. R. Wolpaw and G. Pfurtscheller, "Conversion of EEG activity into cursor movement by a brain–computer interface (BCI)," *IEEE Transaction on Neural Systems and Rehabilitation Engineering,* vol. 12, pp. 331–338, 2004.

[11] D. J. McFarland and J. R. Wolpaw, "Sensorimotor rhythm-based brain–computer interface (BCI): feature selection by regression improves performance," *IEEE Transaction on Neural Systems and Rehabilitation Engineering,* vol. 13, pp. 372–379, 2005.

[12] G. Schalk, G. D. J. McFarland, T. Hinterberger, N. W. Birbaumer and J. R. Wolpaw, "BCI2000: a general-purpose brain–computer interface (BCI) system," *IEEE Transaction on Biomedical Engineering,* vol. 51, pp. 1034–1043, 2004.

[13] L. R. Hochberg, M. D. Serruya, G. M. Friehs, J. A. Mukand, M. Saleh, A. H. Caplan, A. Branner, D. Chen, R. D. Penn, and J. P. Donoghue, "Neuronal ensemble control of prosthetic devices by a human with tetraplegia," *Nature*, vol. 442, no. 13, pp. 164–171, 2006.

[14] S. Kanoh, Y. Murayama, K. Miyamoto et al, "A NIRS-based Brain Computer Interface System during Motor Imagery: System Development and Online Feedback Training", *31st Annual international Conference of the IEEE EMBS*, 2009, pp 594-597.

[15] S. Fazli, J.Mehnert, J. Steinbrink et al., "Enhanced performance by a hybrid NIRS-EEG brain computer interface," *Neuroimage*, vol. 59, pp. 519–529, 2011.

[16] O. Al Zoubi, I. Koprinska and R. A. Calvo, "Classification of brain-computer interface data," *In Proceedings of the 7th Australasian Data Mining Conference, Australian Computer Society*, Inc., vol. 87, pp. 123-131, 2008.

[17] X. Lei, P. Yang, and D. Yao, "An empirical Bayesian framework for brain–computer interfaces." *IEEE Transactions on Neural Systems and Rehabilitation Engineering*, vol. 17, pp. 521-529, 2009.

[18] V. N. Vapnik, The Nature of Statistical Learning Theory, New York: Springer Science and Business Media, 2013.

[19] S. Zhang, "KNN-CF Approach: Incorporating Certainty Factor to k-NN Classification," *IEEE Intel Informatics Bulletin*, vol. 11, pp. 24-33, 2010.

[20] C. C. Liu and F. C. Chen, "Adaptive control of non-linear continuous-time systems using neural networks—General relative degree and MIMO cases," *International Journal of Control*, vol. 58, pp. 317-335, 1993.

[21] S. I. Niculescu and A. M. Annaswamy, "An adaptive Smith-controller for time-delay systems with relative degree $n^* \leq 2$," *Systems and control letters*, vol. 49, pp. 347-358, 2003.

[22] R. J.Vaccaro, Digital Control: A State-Space Approach, McGraw-Hill, New York, NY, 1995.

[23] J. Yue, Z. Zhou, J. Jiang, Y. Liu and D. Hu, "Balancing a simulated inverted pendulum through motor imagery: An EEG-based real-time control paradigm," *Neuroscience letters*, vol. 524, pp. 95-100, 2012.

[24] E. J. Rechy-Ramirez and H. Hu, "Bio-signal based control in assistive robots: A survey," *Digital Communications and Networks, 2015*.

MANUSCRIPT 1

Emulating Conventional Disc Electrode with the Outer Ring of the Tripolar Concentric Ring Electrode in Phantom and Human Electroencephalogram Data

by

Oleksandr Makeyev[1], Yacine Boudria[1], Zhenghan Zhu[1],

Thomas Lennon[1], and Walter G. Besio[1]

Published in IEEE Signal Processing in Medicine and Biology Symposium, New York City, vol. 7, 4 pp, 2013.

---

[1] Oleksandr Makeyev, Yacine Boudria, Zhenghan Zhu, Thomas Lennon, and Walter G. Besio are with Department of Electrical, Computer and Biomedical Engineering, University of Rhode Island, Kingston, RI, 02881, Email: omakeyev@ele.uri.edu, yaciboud@gmail.com,zhu.zhenghan1987@gmail.com,thomas_lennon03@my.uri.edu, besio@ele.uri.edu.

Abstract

Conventional electroencephalography (EEG) with disc electrodes has major drawbacks including poor spatial resolution, selectivity and low signal-to-noise ratio that critically limit its use. Concentric ring electrodes are a promising alternative with potential to improve all of the aforementioned aspects significantly. In our previous work, the tripolar concentric ring electrode (TCRE) was successfully used in a wide range of applications demonstrating its superiority to conventional disc electrodes, in particular, in accuracy of Laplacian estimation (tEEG). For applications that may benefit from simultaneous recording of EEG and tEEG, in this paper we propose to use the signal from the outer ring of the TCRE as an emulation (eEEG) of EEG recorded using conventional disc electrodes. This will allow us to record EEG emulation from the exact same locations at the exact same time as the tEEG using a single recording system. Time domain neuronal signal synchrony was measured using cross-correlation in phantom and human experiments suggesting the potential of eEEG as an emulation of EEG ($r \geq 0.99$).

1.1 Introduction

Electroencephalography (EEG) is an essential tool for brain and behavioral research and is used extensively in neuroscience, cognitive science, cognitive psychology and psychophysiology. EEG is also one of the mainstays of hospital diagnostic procedures and pre-surgical planning. Despite scalp EEG's many advantages end users struggle with its poor spatial resolution, selectivity and low

signal-to-noise ratio, which are EEG's biggest drawbacks and major hindrances in its effectiveness critically limiting the research discovery and diagnosis [1]-[3].

EEG's poor spatial resolution is primarily due to (1) the blurring effects of the volume conductor with disc electrodes; and (2) EEG signals having reference electrode problems as idealized references are not available with EEG [2]. Interference on the reference electrode contaminates all other electrode signals [2]. The application of the surface Laplacian (the second spatial derivative of the potentials on the body surface) to EEG has been shown to alleviate the blurring effects enhancing the spatial resolution and selectivity [4]-[6], and reduce the reference problem.

While several methods were proposed for estimation of the surface Laplacian through interpolation of potentials on a surface and then estimating the Laplacian from an array of disc electrodes [5]-[9], concentric ring electrodes (CRE) have shown more promise. The CREs can resolve the reference electrode problems since they act like closely spaced bipolar recordings [2]. Moreover, CREs are symmetrical alleviating electrode orientation problems [10]. They also act as spatial filters enhancing the high spatial frequencies [10], [11]. Finally, bipolar CREs, consisting of just two elements including a single ring and the central disc, improve the radial attenuation of the conventional disc electrode from $1/r^3$ to $1/r^4$ with higher numbers of poles having the potential to enhance radial attenuation even further [12].

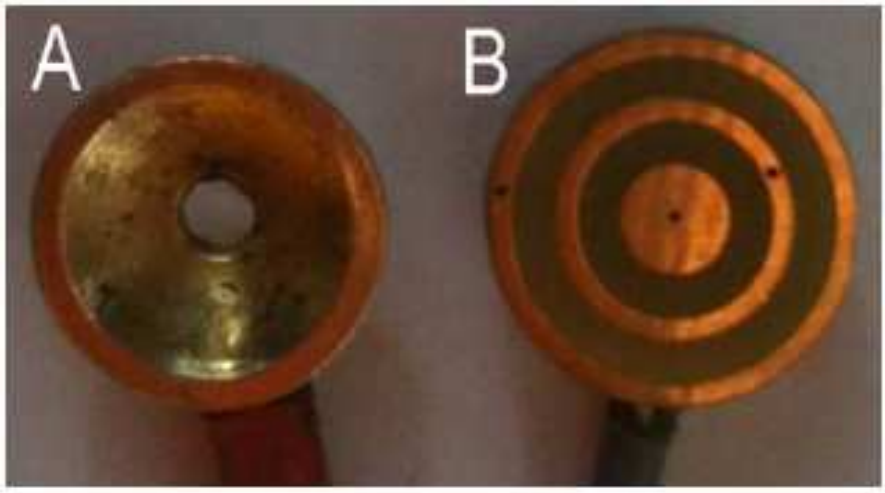

Figure 1.1 Conventional disc electrode (A) and tripolar concentric ring electrode (B)

Tripolar CREs (TCRE), consisting of three elements including the outer ring, the middle ring, and the central disc (Figure 1.1, B), are distinctively different from conventional disc electrodes that have a single element (Figure 1.1, A). TCREs have been shown to estimate the surface Laplacian directly through the nine-point method, an extension of the five-point method used for bipolar CREs, significantly better than other electrode systems including bipolar and quasi-bipolar CREs [13], [14]. The Laplacian algorithm is two-dimensional and weights the middle ring and central disc signal difference sixteen times greater than the outer ring and central disc signal difference [13], [14]. Compared to EEG with conventional disc electrodes, Laplacian EEG using TCREs (tEEG) have been shown to have significantly better spatial selectivity (approximately 2.5 times higher), signal-to-noise ratio (approximately 3.7 times higher), and mutual information (approximately 12 times lower) [15]. TCREs

also have very high common mode noise rejection providing automatic artifact attenuation, -100 dB one radius from the electrode [14]. Because of such unique capabilities TCREs have found numerous applications in a wide range of areas including brain-computer interface [16], seizure attenuation using transcranial focal stimulation applied via TCREs [17]-[20], seizure onset detection in animal models [21], [22] and, most recently, humans [23], etc.

Some current and future applications may require simultaneous recording of EEG using conventional disc electrodes and tEEG. For example, in [23] EEG and tEEG were recorded simultaneously from human patients with epilepsy to allow a direct comparison of seizure onset detection results for two sensor modalities. In [23] EEG and tEEG data were recorded by placing a set of TCREs directly behind the conventional disc electrodes that were in the standard 10-20 system locations but this approach has two disadvantages. First, EEG and tEEG are not being recorded at exactly the same locations. Second, this approach may require additional hardware as two recording systems may have to be used at the same time for EEG and tEEG data respectively (as was done in [23]) resulting in imperfect synchronization in time between EEG and tEEG.

In this preliminary study, we propose to use the signal from the outer ring of TCRE as an emulation (eEEG) of EEG recorded using conventional disc electrodes. This will allow us to record eEEG from the exact same locations at the exact same time as the tEEG using a single recording system. Time domain neuronal signal synchrony was measured using cross-correlation in phantom and human experiments to assess the potential of eEEG as an emulation of EEG. Moreover, in the phantom

experiments, a shorted TCRE was also assessed as an alternative potential emulation of EEG. TCREs with diameter of 1.0 cm (Figure 1.1, B) were used in all of the experiments.

1.2 Methods

1.2.1 Phantom Experiments

A diagram of the setup used for the phantom data collection is presented in Figure 1.2. Three electrodes including the conventional disc electrode and two modified TCREs, one connected as the outer ring and the other one as shorted disc, were placed on a copper plate (Figure 1.2, A) covered by a 3mm layer of Ten20 EEG conductive paste (Figure 1.2, B) (Weaver and Company, Aurora, CO). The copper plate was made from a single sided copper cladded printed circuit board used as a cathode with a smaller round copper plate (Figure 1.2, C) used as an anode and located in such a way that the three electrodes under test were located across two perpendicular diameters of the anode circle at a constant distance of 2mm from it (Figure 1.2, D, E, and F). The cathode and anode were connected to a signal generator producing a sinusoidal wave with frequency of 30Hz and amplitude of 2.5V. Signals from three electrodes were digitized at 16-bit using a USB-2527 data acquisition card (Measurement Computing, Norton, MA) with sampling frequency of 1000Hz and duration of all the recordings equal to 30s.

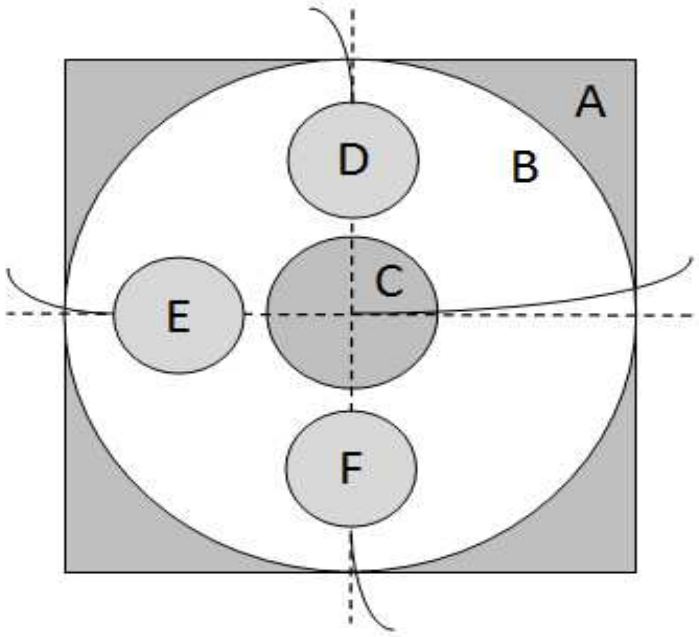

Figure 1.2 Diagram of the setup used for the phantom data collection including: copper cathode plate (A), layer of Ten20 EEG conductive paste (B), copper anode plate (C), and three electrode locations (D, E, and F).

We recorded a total of 10 series, each series consisting of 6 recordings corresponding to six possible combinations of positioning three electrodes at three different locations around the circular anode, to improve the statistical validity of the results. Using all possible positioning combinations at each series of recordings was meant to compensate for the variability due to location. For each series the order of recordings was randomized to balance out the potential effect of the temporal factor. Anode and cathode corrosion were cleaned after each series of recordings.

1.2.2 Human Experiments

The human data were collected from six healthy subjects (1-6, ages 24-40, one female). Baseline brain activity was recorded with the subjects seated in a chair and

asked to remain motionless during the recording process to reduce movement induced artifacts. Durations of individual recordings ranged from 110s to 550s for a total duration of 1730s for 6 subjects which, when subdivided into non-overlapping segments of 10s resulted in 173 segments total for this part of the study. The conventional disc electrode and a TCRE, recording both outer ring signal and Laplacian tEEG, were side-by-side at location P4 of the standard 10-20 system with reference and ground located on the right mastoid process. Skin-to-electrode impedances were maintained below 5kΩ. Signals from the TCRE were preamplified using a custom preamplifier with a gain of 6 after which both TCRE and conventional EEG signals were band pass filtered (0.1-100Hz) and digitized at 1200Hz using a gUSB amplifier with normalized unit gain (g.tec medical engineering GmbH, Schiedlberg, Austria).

1.2.3 Signal Processing and Synchrony Measure

All the signal processing was performed using Matlab (Mathworks, Natick, MA). Sixty 30s recording segments for the phantom data part of this study and 173 10s recording segments from 6 subjects for the human data part of this study were digitally filtered (zero-phase fifth-order Butterworth) with band pass of 1-100Hz and 60Hz notch filter active since this frequency range is the current clinical standard for EEG recording and, therefore, is the primary goal for EEG emulation. Next, cross-correlation, a widely used linear measure of neuronal signal synchrony in the time domain was applied to all the respective pairs of signals from different electrode modalities [24]. For cross-correlation the signals were normalized to zero mean and

unit variance. We calculated both the correlation coefficient at lag zero as well as the maximum correlation coefficient value corresponding to the optimal lag to account for possible time delay between the acquired signals.

1.2.4 Statistical Analysis

For the phantom data, statistical tests were used to assess significance of difference between the two proposed EEG emulation options: eEEG via the TCRE outer ring and shorted TCRE signals. First, we calculated average cross-correlation coefficients for each of 10 series of recordings averaging together coefficients for 6 recordings that comprised each series. Next, we applied unpaired or "independent samples" tests to samples of series cross-correlation coefficients (n = 10) between EEG vs. eEEG and EEG vs. shorted TCRE signal respectively: parametric two-sample Student's t-test (alternative hypothesis of sample means being not equal) and nonparametric Mann–Whitney test (alternative hypothesis of sample medians being not equal) [25]. The Ryan–Joiner (similar to Shapiro–Wilk) normality test was used for all the samples compared [26]. A parametric test was used only when both samples to be compared were normally distributed. Otherwise, a nonparametric test was used.

1.3 Results

1.3.1 Phantom Data

At lag zero the following cross-correlation coefficients (r) were obtained (average ± standard deviation) for 10 series of recordings: for EEG vs. eEEG, r = 0.9744 ±

0.0121; for EEG vs. shorted TCRE signal, r = 0.9445 ± 0.0281. There was a statistically significant difference between the two (p = 0.009).

Individual optimal lags varied between the recordings. Group average optimal lag was equal to one both for EEG vs. eEEG and for EEG vs. shorted TCRE signal. The maximum cross-correlation (*rmax*) corresponding to the unit optimal lag was higher than cross-correlation at lag zero (r) both for EEG vs. eEEG with *rmax* = 0.9841 ± 0.012 (p = 0.045) and for EEG vs. shorted TCRE signal with *rmax* = 0.9766 ± 0.0195 (p = 0.013). There was no statistically significant difference between the two maximum cross-correlations (p = 0.385).

1.3.2 Human Data

At lag zero the following cross-correlation coefficients were obtained (average ± standard deviation) for EEG vs. eEEG on data from 6 subjects r = 0.9905 ± 0.0065. At optimal lag the maximum cross-correlation coefficients were equal to the zero lag coefficients suggesting that there was no time delay between the acquired signals.

1.4 Discussion

Significance of difference between zero lag (r) and optimal lag cross-correlation (*rmax*) coefficients for both EEG vs. eEEG and EEG vs. shorted TCRE signal in phantom data suggests presence of a time delay between the acquired signals the source of which needs be determined. Difference between optimal lags for individual recordings suggests that this delay is variable so group optimal lag that was reported in this study provides a lower bound for the maximum correlation. For example, recalculating the maximum correlation allowing individual lags of up to one sample

(that is, choosing either zero or unit lag for each recording) increases *rmax* both for EEG vs. eEEG with *rmax* = 0.9921 ± 0.012 and for EEG vs. shorted TCRE signal with *rmax* = 0.98 ± 0.032. Moreover, allowing optimal lags for individual recordings further increases the maximum correlation to *rmax* = 0.9981 ± 0.001 for EEG vs. eEEG and *rmax* = 0.9977 ± 0.001 for EEG vs. shorted TCRE signal. Taking into account these varying time delays between the acquired signals for the phantom data experiments, the results obtained on both phantom and human data confirm that signals from the outer ring of TCRE correlate well ($r \geq 0.99$) with the conventional disc electrode signals suggesting the potential of eEEG as an emulation of EEG via conventional disc electrodes. This is an intuitive result since a conventional disc electrode is really a cup where there is an outer ring similar to the outer ring of the TCRE (Figure 1.1).

The proposed EEG emulation alternative was to short all three recording surfaces of the TCRE. In the phantom experiments of this study the zero lag cross-correlation between the TCRE outer ring eEEG and conventional disc EEG was significantly higher ($p = 0.009$) than the corresponding cross-correlation for the shorted TCRE signal. This suggests that eEEG may be a closer approximation of disc electrode EEG than the signal from the shorted TCRE even though high maximum cross-correlation coefficients and lack of statistical significance between them suggests that both proposed EEG emulation options are valid. Another important consideration is that recording tEEG simultaneously with a shorted TCRE signal at the same location is difficult since constantly shorting and un-shorting of the three TCRE elements would require a complex multiplexer introducing additional switching noise. On the other

hand, recording eEEG in parallel with tEEG using a single system does not require additional hardware providing researchers and clinicians with the best of both worlds.

This paper represents a first preliminary step toward emulating the conventional disc electrodes using concentric ring electrodes. Further investigation is needed for conclusive proof with short term directions of future work including determining the source of the varying time delay in the phantom data and conduction of a larger human data study. This study should include shorted TCRE (compared to just eEEG and EEG in the current preliminary study) as well as a larger subject population with longer data durations for individual subjects (compared to short recordings from six subjects in the current study). Assessing the effect of subject's movement and induced artifacts on synchrony between EEG and its emulations is another issue that was not addressed in the current study that includes just the baseline activity. Most importantly, more measures of neuronal signal synchrony need to be added to the currently used time domain linear cross-correlation. Linear spectral coherence may be used to assess the synchrony in the frequency domain both in specific frequency bands and averaged across the spectra. Moreover, nonlinear neuronal signal synchrony measures are available including mutual information, transfer entropy, Granger causality, and nonlinear interdependence as well as different indices of phase synchronization such as the mean phase coherence [27].

References

[1] J. E. Desmedt, V. Chalklin and C. Tomberg, "Emulation of somatosensory evoked potential (SEP) components with the 3-shell head model and the problem of 'ghost potential fields' when using an average reference in brain mapping," *Electroencephalography and Clinical Neurophysiology/Evoked Potentials Section*, vol. 77, pp. 243-258, 1990.

[2] P. L. Nunez, R.B. Silberstein, P.J. Cadiush, J.Wijesinghe, A.F.Westdorp, and R. Srinivasan, "A theoretical and experimental study of high resolution EEG based on surface Laplacians and cortical imaging," *EEG and Clinical Neurophysiology*, vol. 90, pp. 40-57, 1994.

[3] G. Lantz, R. Grave de Peralta, L. Spinelli, M. Seeck, and C. Michel, "Epileptic source localization with high density EEG: how many electrodes are needed?" *Clinical Neurophysiology*, vol. 114, pp. 63-69, 2003.

[4] R. Srinivasan, "Methods to Improve the Spatial Resolution of EEG," *Journal of Bioelectromagnetism*, vol. 1, pp. 102-111, 1999.

[5] B. He, "Brain Electrical Source Imaging: Scalp Laplacian Mapping and Cortical Imaging," *Critical Reviews in Biomedical Engineering*, vol. 27, pp. 149-188, 1999.

[6] B. He, J. Lian, and G. Li, "High-resolution EEG: a new realistic geometry spline Laplacian estimation technique," *Clinical Neurophysiology*, vol. 112, pp. 845-852, 2001.

[7] F. Perrin, O. Bertrand, and J. Pernier, "Scalp Current Density Mapping: Value and Estimation from Potential Data," *IEEE Transaction on Biomedical Engineering*, vol. 34, pp. 283-288, 1987.

[8] S. K. Law, P.L Nunez, R.S. Wijesinghe, "High resolution EEG using Spline Generated Surface Laplacians on Spherical and Ellipsoidal Surfaces," *IEEE Transaction on Biomedical Engineering*, vol. 40, pp.145-153, 1993.

[9] F. Babiloni, C. Babiloni, F. Carducci, L. Fattorini, P. Onorati, and A. Urbano, " Spline Laplacian estimate of EEG potentials over a realistic magnet resonance constructed scalp surface model," *EEG and Clinical Neurophysiology*, vol. 98, pp. 363-373, 1996.

[10] D. Farino, and C. Cescon, "Concentric-Ring Electrode systems for Noninvasive detection of single motor unit activity," *IEEE Transaction on Biomedical Engineering*, vol. 48, pp. 1326-1334, 2001.

[11] C. D. Klug, J. Silny, and G. Rau, “Improvement of Spatial Resolution in Surface EMG: A Theoretical and Experimental Comparison of Different Spatial Filters,” *IEEE Transaction on Biomedical Engineering*, vol. 44, pp. 567-574, 1997.

[12] A. Van Oosterom and J. Strackee, "Computing the lead field of electrodes with axial symmetry," *Medical and Biological Engineering and Computing*, vol. 21, pp. 473–481, 1983.

[13] W. Besio, W. Aakula, K. Koka, and W. Dai, "Development of a tri-polar concentric ring electrode for acquiring accurate Laplacian body surface potentials," *Annals of Biomedical Engineering*, vol. 34, pp. 226-235, 2006.

[14] W. Besio, K. Koka, W. Aakula, and W. Dai, "Tri-polar concentric ring electrode development for Laplacian electroencephalography," *IEEE Transaction on Biomedical Engineering*, vol. 53, pp. 926-933, 2006.

[15] K. Koka and W. Besio, "Improvement of spatial selectivity and decrease of mutual information of tri-polar concentric ring electrodes," *Journal of Neuroscience Methods*, vol. 165, pp. 216-222, 2007.

[16] W. Besio, H. Cao, P. Zhou, “Application of tripolar concentric electrodes and pre-feature selection algorithm for brain-computer interface,” *IEEE Transaction on Neural Systems & Rehabilitation Engineering*, vol. 16, pp. 191-194, 2008.

[17] W. Besio, K. Koka, and A. Cole, “Effects of noninvasive transcutaneous electrical stimulation via concentric ring electrodes on pilocarpine-induced status epilepticus in rats,” *Epilepsia*, vol. 48, pp. 2273-2279, December 2007.

[18] W. Besio, X. Liu, L. Wang, A. Medvedev, and K. Koka, “Transcutaneous electrical stimulation via concentric ring electrodes reduced pentylenetetrazole-induced synchrony in beta and gamma bands in rats,” *International Journal of Neural Systems*, vol. 21, pp. 139-149, April 2011.

[19] O. Makeyev, H. Luna-Munguía, G. Rogel-Salazar, X. Liu, W. Besio, "Noninvasive transcranial focal stimulation via tripolar concentric ring electrodes lessens behavioral seizure activity of recurrent pentylenetetrazole administrations in rats," *IEEE Transaction on Neural Systems and Rehabilitation Engineering*, vol. 21, no. 3, pp. 383-390, May 2013.

[20] W. Besio, O. Makeyev, A. Medvedev, K. Gale, "Effects of transcranial focal stimulation via tripolar concentric ring electrodes on pentylenetetrazole-induced seizures in rats," *Epilepsy Research*, vol.105, pp. 42-51, July 2013.

[21] O. Makeyev, X. Liu, H. Luna-Munguía, G. Rogel-Salazar, S. Mucio-Ramirez, Y. Liu, Y. Sun, S. Kay, W. Besio, "Toward a noninvasive automatic seizure control system in rats with transcranial focal stimulations via tripolar concentric ring electrodes," *IEEE Transaction on Neural Systems and Rehabilitation Engineering*, vol. 20, pp. 422-431, July 2012.

[22] A. Feltane, G.F. Boudreaux-Bartels, W. Besio, "Automatic seizure detection in rats using Laplacian EEG and verification with human seizure signals," *Annals of Biomedical Engineering*, vol. 41, no. 3, pp. 645-654, March 2013.

[23] O. Makeyev, Q. Ding, I.E. Martínez-Juárez, J. Gaitanis, S. Kay, W. G. Besio, "Multiple sensor integration for seizure onset detection in human patients comparing conventional disc versus novel tripolar concentric ring electrodes," *35th Annual International Conference of the IEEE Engineering in Medicine and Biology Society (EMBC), Osaka, Japan*, pp. 17-20, July 3-7, 2013.

[24] R. Shiavi, Introduction to Applied Statistical Signal Analysis: Guide to Biomedical and Electrical Engineering Applications. Waltham: Academic, chapter 9,2007, ch. 9.

[25] D. C. Montgomery, Design and Analysis of Experiments. Hoboken: Wiley, chapter 2, 2004.

[26] N. M. Razali and Y. B. Wah, “Power comparisons of Shapiro-Wilk, Kolmogorov-Smirnov, Lilliefors and Anderson-Darling tests,” *Journal of Statistical Modeling and Analytics*, vol. 2, no. 1, pp. 21–33, 2011.

[27] T. Kreuz, “Measures of neuronal signal synchrony,” Scholarpedia, vol. 6, no. 12, p. 11922 (revision #129418), doi:10.4249/scholarpedia.11922, 2011.

MANUSCRIPT 2

Significant improvements in one-dimensional cursor control using Laplacian Electroencephalography over Electroencephalography

by

Yacine Boudria[1], Amal Feltane[1] and Walter G. Besio[1]

Published in Journal of Neural Engineering, vol. 11, no. 3, 2014.

[1] Yacine Boudria, Amal Feltane and Walter G. Besio are with Department of Electrical, Computer and Biomedical Engineering, University of Rhode Island, Kingston, RI, 02881, Email: yaciboud@gmail.com, amal_feltane@my.uri.edu, besio@ele.uri.edu.

Abstract

Objective. Brain–computer interfaces (BCIs) based on electroencephalography (EEG) have been shown to accurately detect mental activities, but the acquisition of high levels of control require extensive user training. Furthermore, EEG has low signal-to-noise ratio and low spatial resolution. The objective of the present study was to compare the accuracy between two types of BCIs during the first recording session. EEG and tripolar concentric ring electrode (TCRE) EEG (tEEG) brain signals were recorded and used to control one-dimensional cursor movements.

Approach. Eight human subjects were asked to imagine either 'left' or 'right' hand movement during one recording session to control the computer cursor using TCRE and disc electrodes.

Main results. The obtained results show a significant improvement in accuracies using TCREs (44%–100%) compared to disc electrodes (30%–86%).

Significance. This study developed the first tEEG-based BCI system for real-time one-dimensional cursor movements and showed high accuracies with little training.

2.1 Introduction

Brain–computer interfaces (BCIs) are systems that detect changes in brain signals related to human intentions, typically translating intention into a control signal to communicate between the brain and the external world such as computer applications [1]. These new communication systems have the potential to substantially increase and improve the quality of life of people suffering from severe motor disabilities including paralysis, and provide a new way for able-bodied people to control computers or other

devices (e.g., robot arm, artificial limb or computer cursor). The most important clinical applications of BCI systems include brain-derived communication in paralyzed and locked-in patients [2, 3] and restoration of motor function in patients with spinal cord injuries [4].

BCIs enable users to control devices with direct brain communication using electroencephalographic (EEG) activity recorded from electrodes placed on the scalp (noninvasive BCI) [5, 6] or with activity recorded from on or within the brain (Invasive BCI) [7, 8]. The EEG is a noninvasive method to monitor brain electrical activity; however EEG signals have low signal to noise ratio (SNR), low spatial resolution, and are contaminated by various artifacts from other sources. These characteristics limit measuring the spatial distribution of brain electrical activity and thus necessitate significant preprocessing [6]. Invasive BCIs face substantial technical difficulties and clinical risks as they require that recording electrodes be implanted in or on the cortex and function well for long periods, with risks of infection and other damages [8].

Recently, improvements have been developed to make EEG more accurate by increasing the spatial resolution. One such improvement is the application of the surface Laplacian to the EEG, the second spatial derivative. Tripolar concentric ring electrodes (TCREs) (see figure 2.1(B)) automatically perform the Laplacian on the surface potentials. Previously we have shown that TCRE EEG (tEEG) has significantly better spatial selectivity, SNR, localization, approximation of the analytical Laplacian, and mutual information than conventional EEG with disc

electrodes [9, 10]. These findings suggest that tEEG may be beneficial for neurological disorders analysis like seizure detection [11, 18].

An important concern in BCI research is to control the computer cursor such as able-bodied persons do. Cursor control requires the subject to learn how to adapt their brain signals by using different thought patterns for different tasks [12]. Studies in recent years have shown that EEG-based BCI has great potential in achieving one-dimension cursor control [13–15]. However, these systems usually require long-term training in regulating brain signals and the performance in long-term use is often not robust [16]. For example, Wolpaw *et al* [6] performed over twenty sessions per subject, at a rate of two to four per week to develop high-accuracy cursor control (i.e., >90%) [6]. Slow training of subjects and low spatio-temporal resolution is still a serious problem [12]. In order to make future BCI convenient, the training time must be reduced without loss of accuracy.

The objective of this research project was to compare the accuracy of one-dimensional ('left'–'right') cursor control between EEG and tEEG. A secondary objective was to determine if high accuracies could be accomplished using only a single training session. We demonstrate that tEEG signals can enable users to learn how to control a one-dimensional computer cursor rapidly and accurately during their first session with significantly higher accuracy when compared to the EEG signals.

The rest of the paper is structured as follows: section 2 presents a general description of the dataset used in this work and the procedure employed is explained in detail. Section 3 presents the obtained results with a general discussion. Finally, some conclusions with future work are offered.

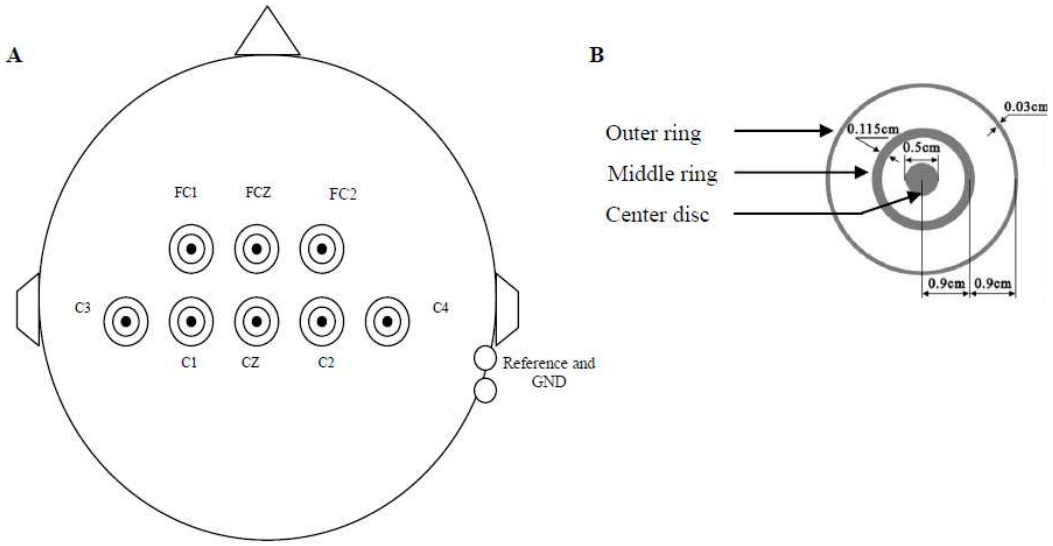

Figure 2.1 (A) Schematic illustration of the electrode montage. The EEG signal is recorded from the outer ring of the TCRE electrodes. EEG and tEEG signals were recorded from the same location concurrently. (B) Schematic of TCRE electrode.

2.2 Methodology

2.2.1 Laplacian Electroencephalography (tEEG)

The scalp surface Laplacian is an alternative method for presenting EEG data with higher spatial resolution. It has been shown that the surface Laplacian is proportional to the cortical potentials and improves the high spatial frequency components of the brain activity near the electrode [19]. To obtain the Laplacian, we take a new approach by using unique sensors and instrumentation for recording the signal [9, 20]. The unique sensor configuration which measures the Laplacian potential directly is the TCRE (Figure 2.1, panel B) [9, 10]. Two differential signals from each electrode were combined algorithmically for a tEEG derivation of the signal as reported previously in

[9]. Briefly, the algorithm is two-dimensional and weights the middle ring and central disc difference sixteen times greater than the outer ring and central disc difference, 16*(middle–disc) – (outer–disc), where disc is the central disc, middle is the middle ring, and outer is the outer ring of the TCRE. The outer ring was used as the disc electrode (Figure 2.1, panel B). In our previous work [22] we have shown that the outer ring signal has a 0.99 correlation to disc electrode signals. All the signal processing was performed using MATLAB (Mathworks, Natick, MA, USA).

2.2.2 Data Recording

The brain signals were gathered from eight healthy subjects (1–8, ages 24–40, two female). The subjects were naive to neuro-feedback training and their task was to use their thoughts to move a cursor, in the form of a ball, from the center of a computer screen to a target. The target was a pink rectangle which appeared in the 'left' or the 'right' of the periphery of the screen. The cursor width was 10% of the screen width. Figure 2.2 shows a screenshot of the real-time application.

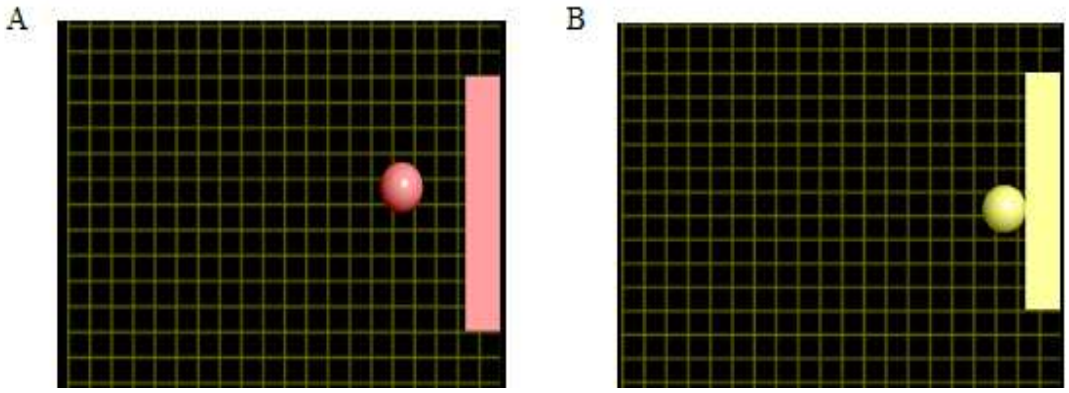

Figure 2.2 Screenshot of the real-time application for cursor control. The ball is the cursor and the rectangle is the target. (A) Before the ball hit the target and (B) when the ball hit the target, the color of the target turned yellow.

During BCI operation, subjects were seated in a chair, facing a computer screen which was placed about 1.5 min front of the subject. The subjects were asked to remain motionless during the recording process to reduce the introduction of artifacts. The BCI2000 [16] software application was used to acquire and process in real-time signals recorded from eight scalp surface electrodes (C3, C1, Cz, C2, C4, FC1, FCz, FC2) according to the international 10–20 system, with reference and ground from the right mastoid process (see Figure 2.1 panel A). Skin-to-electrode impedances were maintained below 5 kΩ. Signals from all the channels were first pre-amplified with a gain of 6, then amplified, filtered (0.1–100 Hz) and digitized (sampling frequency was 256 Hz) with a gUSB amplifier (g.tec GmgH, Schiedlberg, Austria). For a direct comparison between EEG and tEEG cursor accuracy TCREs were placed once and used for both experiments. The subjects were unaware as to whether EEG or tEEG was used for BCI.

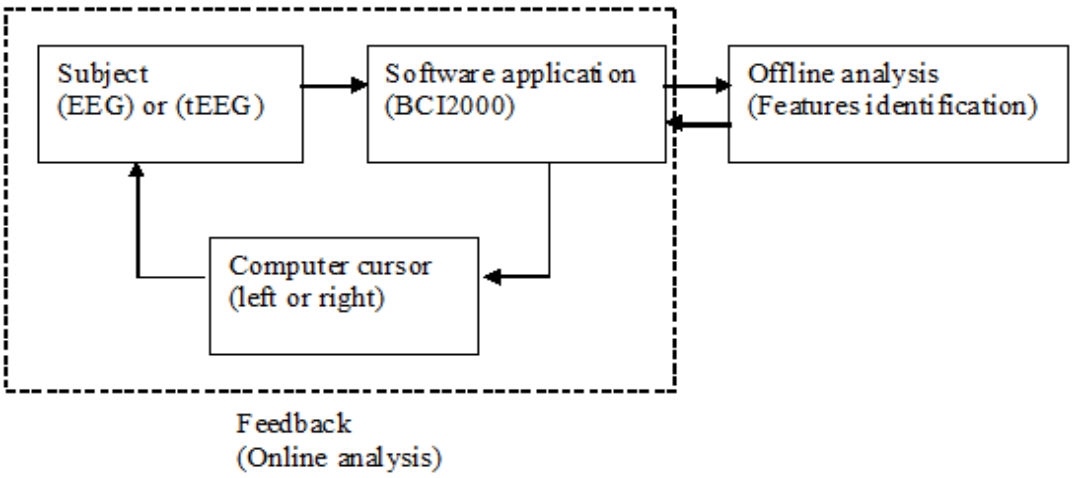

Figure 2.3 Procedure of one-dimensional computer cursor control.

2.3 Procedure

In this paper, for achieving one-dimension cursor control two stages were used: (1) features identification during an offline analysis, and (2) online one-dimensional BCI cursor control (real-time one-dimensional cursor control). The two stages are described in the following section (see Figure 2.3).

2.3.1 Offline Analysis for features identification

The offline analysis was performed to determine which components and features of the signal the user could most easily modulate for BCI control. First we determined which EEG and tEEG features (i.e., signal amplitudes at particular frequency bands and particular electrode locations) were correlated with a particular motor imagery task, and might thus be the basis for BCI experiments.

To measure and characterize responses to motor imagery, each subject had to imagine ‘left’ and ‘right’ hand movements, following a fixed repetitive time scheme of an arrow pointing ‘left’ or ‘right’ for 2 s, and to rest while the screen was blank for 1 s. The appearance of the arrow was random and each ‘left’ or ‘right’ task was repeated ten times. Moreover, the data were collected just for one session (to assure that the subject was a first-time BCI user). The session consisted of five runs, and each run consisted of 20 trials for 100 trials total.

For these analyses, we converted the time-series EEG and tEEG data into the frequency domain, with 2 Hz wide bins from 0 to 140 Hz, using an autoregressive model of order 20 (BCI200 function) to produce a set of frequency spectra for each location and for each task and rest. We then calculated the statistical difference for the

distribution of frequency magnitude at each electrode location and frequency (i.e., values of r^2, which indicated what fraction of the signal variance at that location and frequency was due to the condition of task and rest). This procedure was performed to identify features that could be modulated by the subject using imagined tasks.

Electrodes for each subject were identified for a selected frequency band that exhibited a high correlation with the imagined right hand movement task (i.e. the largest value of r^2) for both EEG and tEEG signals (see Table 2.1). From the feature plot (Figure 2.4) it is observed that the largest r^2 value in the selected frequency band appeared in the C3, C1, and FC1 electrodes located on the left motor cortex (Figure 2.1). Furthermore, we selected up to three electrodes, from the frequency bands that we monitored. An electrode was selected if the r^2 value was dark red ($r^2 > 0.09$). The amplitudes of these features (frequency band and electrode location) were used by the subject to move the cursor to the 'right' toward the target on the screen during the online procedure. During rest the cursor moved to the 'left'.

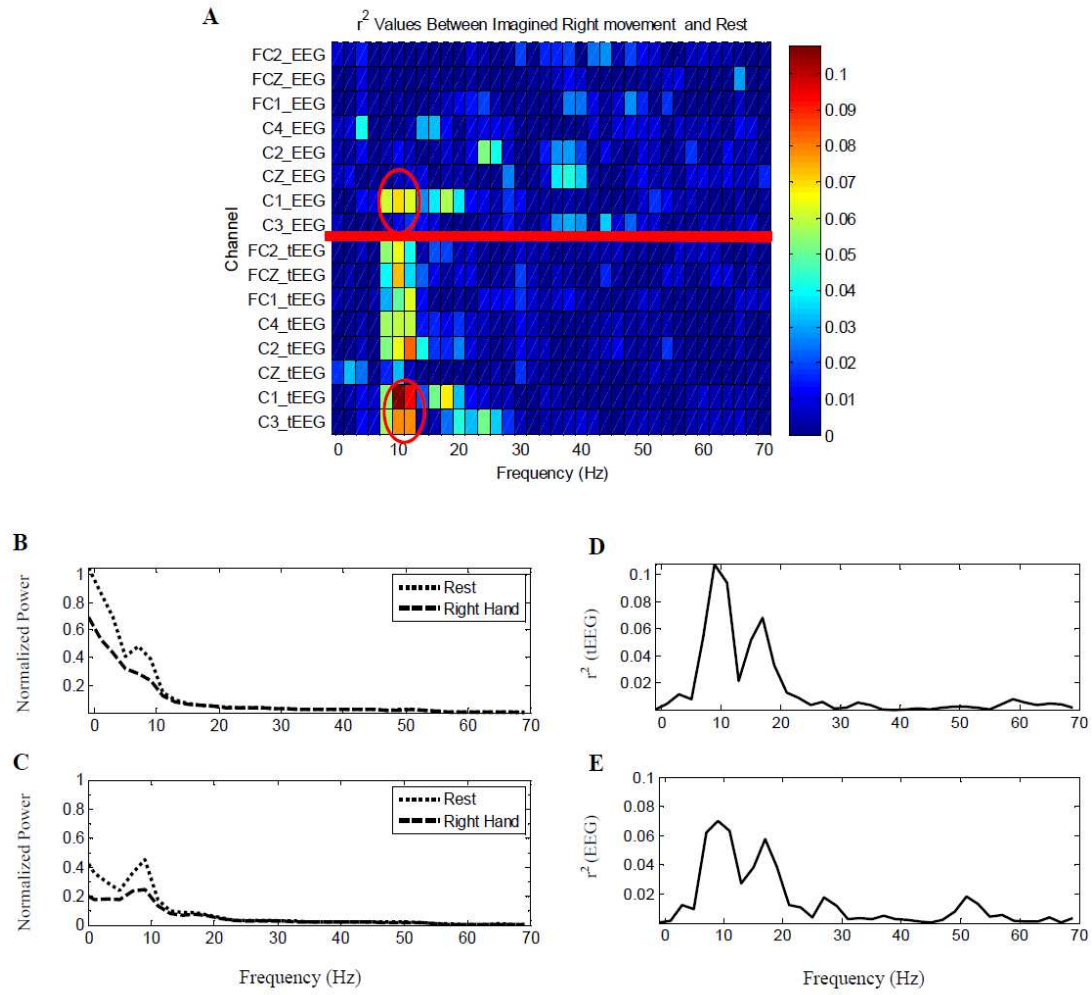

Figure 2.4 Example of an analysis comparing between tEEG and EEG signals for the 'right' hand imaginary and rest. (A) Values of r2 for all the electrodes locations and frequencies for both tEEG and EEG signals. Normalized power from channel C1 for: (B) tEEG and (C) EEG. The corresponding r2 spectrum measures the amplitude variation for (D) tEEG (E) and EEG for electrode C1.

Figure 2.4 shows an example analysis calculated for one subject performing imagined 'right' hand movement and rest. The top panel (A) shows the values of r^2 for each electrode location and frequency bin for both EEG (top half) and tEEG (bottom half) signals. It can be seen that some signals at particular locations and frequencies exhibit a difference between the task and rest such as location C1, which was used for the remainder of Figure 2.4. Panel B shows the average tEEG frequency spectra for 'right' hand movement and rest whereas Panel C shows the same for EEG. Panel D shows the r^2 values for tEEG and Panel E for the EEG. This same process was followed for each subject during a no-feedback session and the features (i.e., electrode locations and frequency band) that had the highest values of r^2 were determined for each subject.

Table 2.1 The average rates of online experimental results for each subject using both EEG and tEEG signals and their corresponding electrode locations and frequency bands for 'right' hand imaginary task.

	Electrode locations		Frequency band (Hz)		Hit accuracy (%)	
Subjects	EEG	tEEG	EEG	tEEG	EEG	tEEG
1	C3, FC1	C1, FC1	8.5–10.5	10.5–12.5	54.8	63.8
2	C3	C1, C3	8.5–10.5	8.5–10.5	44.1	55.1
3	C1, FC1	C1, C3, FC1	8.5–10.5	10.5–12.5	57.7	71
4	C1, C3, FC1	C3	18.5–20.5	16.5–18.5	61.8	72.4
5	C1	C1, C3	8.5–10.5	10.5–12.5	62.9	71
6	C1, C3, FC1	C1, C3, FC1	28.5–30.5	24.5–26.5	66.3	83.5
7	C1, FC1	C1, C3	16.5–18.5	16.5–18.5	60.3	71.6
8	C3	C1, C3	20.5–22.5	16.5–18.5	65.1	73.2

2.3.2 Online Testing

The order of the EEG or tEEG closed-loop control was randomized without the subject knowing which they were performing. The closed-loop BCI experiments, the real time testing, were performed with the subject receiving online feedback. The feedback consisted of one-dimensional cursor imaginary movement controlled by the EEG or tEEG features. Moreover, the subjects received feedback that was proportional to the extracted features identified in the methods of section 3.1. To translate the extracted features into a set of signals that moved the cursor toward the target during the online feedback, the amplitudes of an identified frequency band were summed linearly for the identified electrodes [23]. The weights were chosen so that the cursor moved to the 'right' with task performance and to the 'left' during rest. The weights were selected manually to set this configuration. Initially, we performed a trial task for each subject using EEG and an initial weight value of (1). We monitored the speed of the ball and adjusted the weight so that the cursor moved from the center to the target within 2 s for each subject. The same weights determined for the EEG were also used for the tEEG. The EEG and tEEG features were integrated over time to yield the current cursor position.

The subject's goal was to move the cursor horizontally so that it hit the appropriate (i.e., 'left' or 'right') target. Data were collected from each subject for 10 runs, each run comprised 20 trials. The runs were separated with short breaks. The random 'left' or 'right' target appeared 2 s prior to the cursor (a ball) which appeared in the center of the screen. The trial ended 1 s after a hit, miss, or abort with a total run duration of approximately 8 s. The feedback duration was 2 s with a maximum duration of 4 s.

One session comprised ten runs for approximately 2.7 min per run and approximately 27 min for a session. Data were collected for only one session from each subject. The cursor was visible and controllable throughout the whole run. Once the cursor hit the target, the color changed from pink to green to show the successful performance. Since there were two possible outcomes in each trial, the expected probability in the absence of any control was 0.5.

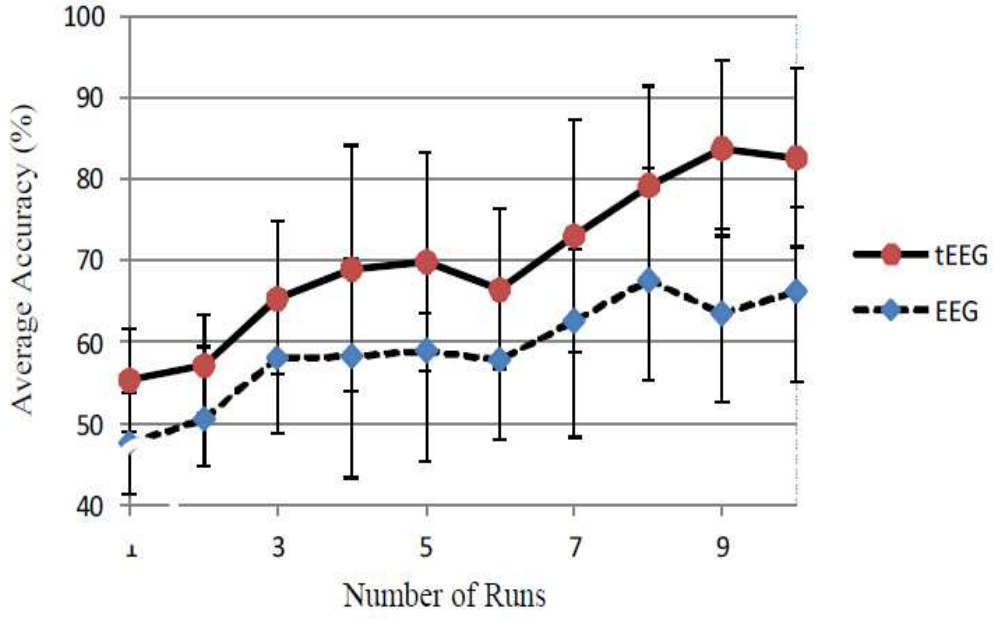

Figure 2.5 Average accuracy for tripolar concentric ring electrode (TCRE) (continuous line) and disc electrode (dashed line). The bar values are mean ± SD (standard deviation).

2.4 Results and Discussion

In this study, we report the first tEEG-based BCI system for one-dimensional real-time cursor movements. Furthermore, we emphasize that the system requires only one training session of an offline analysis for features identification (~27 min) and online testing (~27 min) resulting in proficient operation. The procedure for achieving one-dimensional cursor control had two stages. In the first stage, the data were collected from naıve subjects and analyzed using an offline process to determine which features could be used for BCI control. In the second stage, the subjects attempted to control of the computer cursor.

During offline analysis, the signal amplitudes related to the electrodes location and frequency bands with the most significant task (i.e., the highest values of r^2) were identified as features to be used to control cursor movement in the subsequent online BCI experiments. The r^2 is a measure of how relevant a signal is to the presented target [21]. An analysis example comparing tEEG and EEG signals for the right-hand imaginary and rest is shown in Figure 2.4. The analysis of r^2 (Figure 2.4 panel D and panel E) demonstrate that the relevant signal is focused in the mu and beta frequency bands. Moreover, Figure 2.4 panel B and C shows that the normalized power of these frequency bands decreased during task execution.

In the online analysis, the subjects controlled a cursor (moving the cursor to the left or right edge of the screen to hit the target) with their EEG or tEEG signals. The obtained accuracies are comparable to other noninvasive and invasive BCI studies aimed at one-dimensional cursor control [6, 8, 17 and 21]. For examples in [6], human subjects try to control at first a one-dimensional movement and then moved to a two

dimensional movement using a noninvasive BCI. The tasks were performed from 2–4 times a week with a 92% hit rate achieved. In [17], the subjects controlled a cursor in one dimensional direction by imagined movements. All data of each subject were recorded on the same day without subject training. The average accuracy of all subjects obtained online in the feedback application was 90.5%.

Over short training periods (~27 min), all eight users achieved significant control of the computer cursor. Figure 2.5 shows the average group accuracy during online cursor control obtained from each user for the period of ten runs. The average rates of online experimental results for each subject using both disc and tripolar electrodes are shown in Table 2.1. The maximum hit rate reached 86% using EEG (Subject 4) and reached 100% using tEEG (Subjects 3 and 6). The overall average hit rate and standard deviation for EEG and tEEG was 59.1% ± 7.13 and 70.2% ± 8.13, respectively (Figure 2.5). One-way analysis of variance (ANOVA) with blocking factor levels corresponding to eight human subjects was used to confirm that there was a significant difference in the mean BCI hit rate between data corresponding to conventional disc EEG and tripolar concentric ring Laplacian tEEG ($p < 0.0001$). These results show that there is a significant difference in accuracy of the tEEG to disc EEG for new users in real-time one-dimensional cursor control.

Comparing the obtained results from EEG and tEEG signals, the cursor control accuracy using tEEG, on average, was significantly higher than for the disc EEG. When moving the cursor in one dimension, two of the eight subjects were able to hit 100% of the targets within one session (~27 min) using tEEG. We believe that this increased accuracy in a shortened time will help users train on the BCI quicker.

We always used the features that provided the highest r^2 for each electrode type. Many times the electrode locations used for EEG and tEEG overlapped and sometimes the frequency bands also overlapped. Although, the performance of tEEG over EEG may be partially due to different selection of features, we believe this improvement is also due to tEEG having higher spatial resolution, lower mutual information, and better SNR than EEG which provides more specific features.

2.5 Conclusion

In this paper, we have shown a significant improvement in accuracy for one-dimensional BCI real-time center out cursor control using tEEG compared to EEG in humans after minimal training. The obtained results indicate that tEEG-based BCI could provide one-dimensional control that is more accurate with shorter training time requirements than EEG-based BCI. All eight subjects demonstrated reliable control achieving an average of 70.2% using tEEG-based BCI and an average of 59.1% using EEG-based BCI after only one offline training session. As a result, the average improvement of the tEEG-based BCI over the EEG-based BCI was more than 15%. Using TCREs allowed us to collect the tEEG and EEG data from the same locations at the same time for comparison.

Our future studies will focus on two-dimensional cursor control to determine the hit accuracies for tEEG and EEG signals.

References

[1] J. R. Wolpaw, N. Birbaumer, D. McFarland, G. Pfurtscheller and T. Vaughan, "Brain–computer interfaces for communication and control," *Clinical Neurophysiology,* vol. 113, pp**.** 767–791, 2002.

[2] N. Birbaumer, N. Ghanayim, T. Hinterberger, I. Iversen, B. Kotchoubey and A. Kubler, "A spelling device for the paralyzed," *Nature,* vol. 398, pp. 297–298, 1999.

[3] C. Neuper, G. Muller, A. Kubler, N. Birbaumer and G. Pfurtscheller, "Clinical application of an EEG-based brain–computer interface: a case study in a patient with severe motor impairment," *Clinical Neurophysiology,* vol. 114, pp. 399–409, 2003.

[4] G. R. M¨uller-Putz, R. Scherer, G. Pfurtscheller and R. Rupp, "EEG-based neuroprosthesis control: a step into clinical practice," *Neuroscience Letter,* vol. 382, pp. 169–174, 2005.

[5] J. J. Vidal, "Real-time detection of brain events in EEG," *Proceedings of the IEEE,* (special issue on biological signal processing and analysis), vol. 65, pp. 633–664, 1997.

[6] J. R. Wolpaw and D. J. McFarland, "Control of a two-dimensional movement signal by a noninvasive brain–computer interface in humans," *Proceedings of the National Academy of Science of the United States of America,* vol. 101, pp. 17849–17854, 2004.

[7] T. N. Lal, T. Hinterberger, G. Widman, M. Schrioder, N. J. Hill, W. Rosenstiel, C. E. Elger, K. Sch¨olkopf and N. Birbaumer, "Methods towards invasive human brain–computer interfaces," *Advances in Neural Information Processing Systems,* (Cambridge, MA: MIT Press), vol. 17, pp. 737–744, 2004.

[8] E. C. Leuthardt, G. Schal, J. R. Wolpaw, J. G. Ojemann and D. Moran, "A brain–computer interface using electrocorticographic signals in humans," *Journal of Neural Engineering,* vol. 1, pp. 63–71, 2004.

[9] W. Besio, K. Koka, R. Aakula and W. Dai, "Tri-polar concentric electrode development for high resolution EEG Laplacian electroencephalography using tri-polar concentric ring electrodes," *IEEE Transaction on Biomedical Engineering (BME),* vol. 53, pp. 926–933, 2006.

[10] K. Koka and W. Besio, "Improvement of spatial selectivity and decrease of mutual information of tri-polar concentric ring electrodes," *Journal of Neuroscience Methods,* vol. 165, pp. 216–222, 2007.

[11] A. Feltane, G. F. Boudreaux-Bartels and W. Besio, "Automatic seizure detection in rats using Laplacian EEG and verification with human seizure signals," *Annals of Biomedical Engineering,* vol. 41, pp. 645–654, 2013.

[12] A. Kostov and M. Polak, "Parallel man-machine training in development of EEG based cursor control," *IEEE Transaction on Rehabilitation Engineering,* vol. 8, pp. 203–4, 2000.

[13] M. Cheng, W. Y. Jia, X. R. Gao,S. K. Gao and F. S. Yang, "Mu-rhythm-based cursor control: an offline analysis," *Clinical Neurophysiology,* vol. 115, pp. 745–51, 2004.

[14] G. E. Fabiani, D. J. McFarland, J. R. Wolpaw and G. Pfurtscheller, "Conversion of EEG activity into cursor movement by a brain–computer interface (BCI)," *IEEE Transaction on Neural Systems and Rehabilitation Engineering,* vol. 12, pp. 331–338, 2004.

[15] D. J. McFarland and J. R. Wolpaw, "Sensorimotor rhythm-based brain–computer interface (BCI): feature selection by regression improves performance," *IEEE Transaction on Neural Systems and Rehabilitation Engineering,* vol. 13, pp. 372–379, 2005.

[16] G. Schalk, G. D. J. McFarland, T. Hinterberger, N. W. Birbaumer and J. R. Wolpaw, "BCI2000: a general-purpose brain–computer interface (BCI) system," *IEEE Transaction on Biomedical Engineering,* vol. 51, pp. 1034–1043, 2004.

[17] B. Blankertz, G. Dornhege, M. Krauledat, K. R. Muller, V. Kunzmann, F. Losch and G. Curio, "The Berlin brain–computer interface: EEG-based communication without subject training," *IEEE Transaction on Neural Systems and Rehabilitation Engineering,* vol. 14, pp. 147–52, 2006.

[18] A. Feltane, G. F. Boudreaux Bartels, Y. Boudria and W. Besio, "Seizure detection using empirical mode decomposition and time-frequency energy concentration," *SPMB'13: IEEE Signal Processing in Medicine and Biology Symposium,* pp 1–6, 2013.

[19] F. Babiloni, C. Babiloni, L. Fattorini, F. Carducci, P. Onorati and A. Urbano, "Performances of surface Laplacian estimators: a study of simulated and real scalp potential distributions," *Brain Topography, vol.* 8, pp. 35–45, 1995.

[20] W. Besio, H. Cao and P. Zhou, "Application of tripolar concentric electrodes and pre-feature selection algorithm for brain–computer interface," *IEEE Transaction on Neural Systems and Rehabilitation Engineering,* vol. 16, pp. 191–4, 2008.

[21] J. R. Wolpaw, D. McFarland, G. Neat and C. Formeris, "An EEG based brain–computer interface for cursor control," *Electroencephalography and Clinical Neurophysiology,* vol. 78, pp. 252–259, 1991.

[22] O. Makeyev O, Y. Boudria Y, Z. Zhu, T. Lennon and W. Besio, "Emulating conventional disc electrode with the outer ring of the tripolar concentric ring electrode in phantom and human electroencephalogram data," *SPMB'13: IEEE Signal Processing in Medicine and Biology Symposium,* 4 pp., 2013.

[23] D. J. McFarland and J. R. Wolpaw, "EEG-based communication and control: speed-accuracy relationships," *Applied Psychophysiology and Biofeedback, vol.* 28, pp. 217–231, 2003.

MANUSCRIPT 3

Imagery Tasks Classification using Laplacian EEG and NIRS based BCI

by

Yacine Boudria[1], Rand K. Almajidy[2,3,4], Amal Feltane[1], Richard J. Vaccaro[1], Kunal Mankodiya[1], Ulrich G. Hofmann[2], Walter G. Besio [1]

To be submitted to Journal of Neural Engineering

---

[1] Yacine Boudria, Amal Feltane and Richard J. Vaccaro, Kunal Mankodiya and Walter G. Besio are with Department of Electrical, Computer and Biomedical Engineering, University of Rhode Island, Kingston, RI, 02881, Email: yaciboud@gmail.com, amal_feltane@my.uri.edu, besio@ele.uri.edu.

[2] Neuroelectronic Systems, Dept. of Neurosurgery, University of Freiburg Medical Center, Freiburg, Germany; Email: almajidy@klinikum.uni-freiburg.de, ulrich.hofmann@uniklinik-freiburg.de.

[3] Institute for Signal Processing, University of Luebeck, Luebeck, Germany;

[4] College of Medicine, University of Diyala, Diyala, Iraq.

Abstract

Electroencephalogram (EEG) based brain–computer interface, (EEG-based BCI), has attracted much attention since it provides a new communication channel between the human brain and the computer. Recent studies have demonstrated that near-infrared spectroscopy (NIRS) is a promising neuroimaging modality for BCIs. In the present study, we evaluated the performances of a variety of imagery mental task combinations which are right, left, up and down using: Laplacian tripolar EEG (tEEG) and NIRS based BCIs. To this end, we recorded the tEEG signal and the event-related hemodynamic responses from nine participants while performing these imagery tasks. Classification accuracies were then estimated comparing these four mental tasks with rest using two different classifiers, the support vector machine (SVM) and the k-nearest neighbor (k-NN) algorithm.

3.1 Introduction

A brain–computer interface (BCI) translates electrical signals detected from the brain to control an output device which can help those suffering from neuromuscular impairments to interact and communicate with their surrounding environment [1]. BCIs can be invasive or non-invasive. Invasive BCIs read the user's intent from neuronal action using electrodes embedded on or directly within the brain. Non-invasive BCIs derive the user's intent from neuronal action recorded from the scalp. Many noninvasive methods have been developed to examine brain activity, for example Electroencephalography (EEG) [2-4], Laplacian tripolar EEG (tEEG) [14],

magnetoencephalography (MEG) [5], functional magnetic resonance imaging (fMRI) [6, 7] and near-infrared spectroscopy (NIRS) [8-10].

EEG is the measurement and recording of the brain electrical activity using sensors arrayed across the scalp. Surface EEG has many advantages. For example, it is non-invasive, has a good temporal resolution and available at low cost. However, EEG has low signal-to-noise ratio and low spatial resolution that does not allow an accurate localization [11]. Recently, improvements have been applied to EEG recording techniques making it more accurate by increasing the spatial resolution. One such improvement is the application of the surface Laplacian to the EEG [12, 13]. The tripolar concentric ring electrodes (TCREs), (see Figure 3.3 panel B) were used to record the tEEG. It has been shown that tEEG has significantly better spatial resolution and better signal-to-noise ratio than EEG recorded using the traditional disc electrodes [12, 13]. In our previous work [22], we found a significant improvement in detection of single event imagined movements with tEEG compared to EEG. Recently we found a significant improvement in real-time 1D cursor control accuracy using tEEG compared to EEG [14].

Near-infrared spectroscopy (NIRS) is a non-invasive optical imaging technique used to acquire brain signals by transmitting near-infrared (650 nm – 950 nm wavelengths) electromagnetic radiation through the skull and comparing the intensities of the returning and incident light. During mental activity, an increase in the blood flow to pre-defined regions of the brain is observed, e.g., motor cortex during motor imagery tasks [15, 16]. The increase in blood flow causes changes to the regional concentrations of oxygenated and deoxygenated hemoglobin [8]. Near-infrared

spectroscopy provides researchers with a variety of advantages such as flexibility of use, good spatial and temporal resolution, localized information, affordability and high sensitivity in detecting small substance concentration [11]. Moreover, NIRS is much less sensitive to EMG artifacts than EEG. It has also been shown that NIRS has some disadvantages such as slow operation due to the inherent latency of the hemodynamic response and weak signal due to hair on the head which may introduce artifacts. Coyle et al. 2004 [8] were one of the first to explore the feasibility of NIRS for a BCI system. Recently, NIRS-based brain-computer interfaces were introduced for discriminating motor tasks imagery by different studies [8, 9, 19-21].

The goal of our study was to investigate the potential of classifying different imagery tasks using tEEG and NIRS based BCI. The imagery tasks were, left-hand motor imagery, right-hand motor imagery, both hands-motor imagery and both-feet motor imagery. During offline analysis, the extracted mean and the median values of tEEG and NIRS signals during task were used as input to two different classifiers, the support vector machine (SVM) [27] and k-nearest neighbor (k-NN) [28]. The block diagram describing the procedure of data acquisition and the control command process is shown in Figure 3.1. In this study we will also discuss online classification towards developing a tEEG–based BCI.

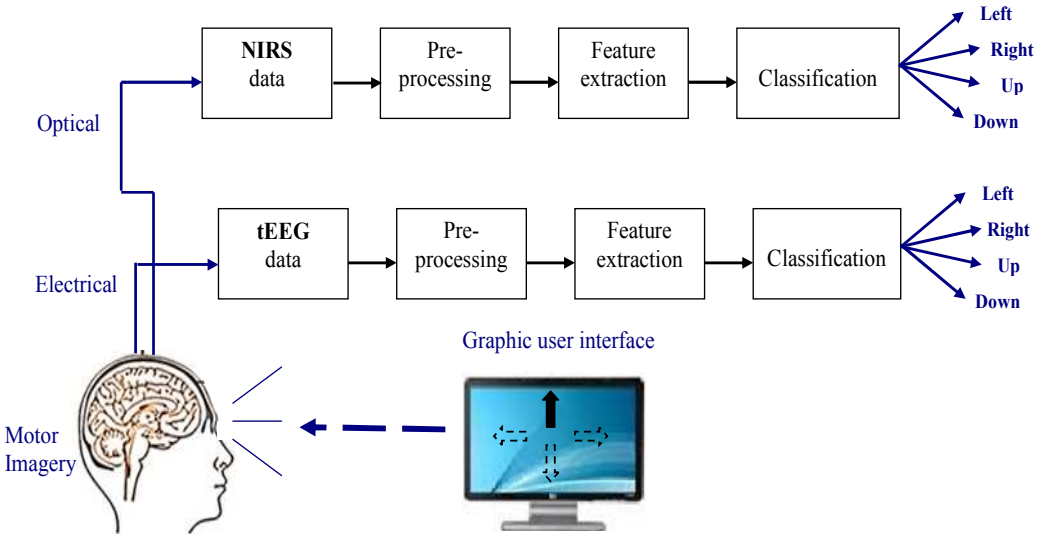

Figure 3.1 Block diagram showing the signal acquisition and the control command process for using brain signals recorded by tEEG and NIRS during motor imagery.

3.2 Materials and Procedures

3.2.1 Subjects and Experimental Paradigm

Nine healthy subjects (20 to 36 years old) voluntarily participated in this study. All subjects signed a University of Rhode Island Institutional Review Board approved informed consent. None of the subjects had a previous neurological history or other severe diseases that might influence the experimental results. The experimental procedure was explained in detail to each subject before the experiment. The experiment was performed in a reduced noise room. Subjects were seated in a chair, facing a computer screen which was placed about 1.5 m in front of them. The subjects were asked to remain motionless during the recording process to reduce the introduction of artifacts.

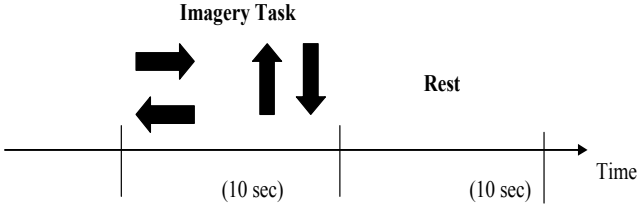

Figure 3.2 Experimental protocols for motor imagery for tEEG and NIRS signals. A black arrow is displayed on the computer screen as one of the four tasks: left, right, up or down to specify the direction for each trial.

To measure and characterize responses to motor imagery, the subject was asked to imagine each of the following selected tasks: 'left hand movement (LI)', 'right hand movements (RI)' or 'both hand movement (BHI)' or 'both feet movement (BFI)', without performing any real motion, for a fixed time duration during which an arrow was pointing left, right, up or down, respectively, for 10 s, and to rest while the screen was blank for 10 s. Figure 3.2 shows the overall experimental paradigm used in this study. Each run was created with an initial period of 10 s to set up a baseline Rest value. Following this baseline Rest period, the subject performed motor task imagery for a period of 10 s. The next 10 s were considered a rest period; the screen was left blank and the subject was asked to relax without any concentration or motion. This pattern was repeated 20 times for each run for a total of 200 trials (10 runs). However, because of very large noise interference and some subject's unexpected movement (artifacts), a few trials were omitted from the processed data after visual inspection.

3.2.2 Data Acquisition

Simultaneous measurements of the brain activities related to mental imagery tasks were performed from tEEG and NIRS recorded data.

Eight surface TCREs were placed on scalp locations: C3, C1, Cz, C2, C4, FC1, FCz, FC2 according to the international 10–20 system [23]; reference and ground were placed on the right mastoid process (see Figure 3.3). Skin-to-electrode impedances were maintained below 5 kΩ. Signals from all the channels were first pre-amplified (gain = 6) then filtered using a band pass filter (0.1–70 Hz) and digitized (sampling frequency was 256 Hz) with a gUSB amplifier (g.tec GmgH, Schiedlberg, Austria). The BCI2000 [24] software application was used to acquire and process signals in real-time.

To record the NIRS data, the NIRS-System (NIR_Scout, NIRX Medical Technologies, USA) was used in this experiment with wavelength of 760 and 850 nm. Figure 3.3 shows the optode configuration used in this study. The illuminator source and detector optodes were placed on the scalp. A total of 8 sources and 8 detectors form a combinational pair of 20 optical path channels that were used in the experiment. The detector optodes were placed at a fixed distance of 3 cm from the illuminator optodes. These optodes were placed on the left and right hemisphere around the C3 and C4 area. The sampling frequency used for the acquisition of NIRS signals was 7.812Hz.

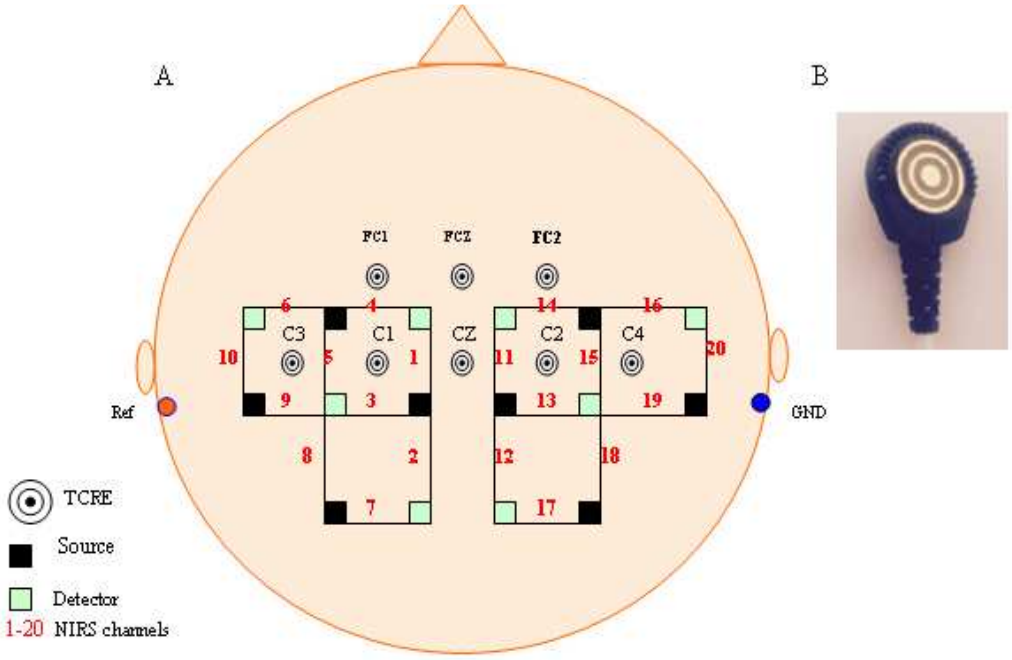

Figure 3.3 tEEG electrodes and NIRS optodes locations. (A) Eight tripolar concentric ring electrodes (TCREs) were used to record the tEEG signal and 20 NIRS channel locations using eight illuminator sources and eight detectors for NIRS. (B) Schematic of tripolar concentric ring electrode (TCRE).

3.2.3 Signal Processing

Further analysis of the NIRS and tEEG offline data were performed as follows. The session was constructed from 10 runs, each run was formed from 20 trials, and the length of each trial was 20 s representing one of the four tasks: (LI), (RI), (BHI), (BFI) and rest that were recorded using both NIRS and tEEG data.

The recorded NIRS signals were converted into oxygenated hemoglobin (HbO_2) and deoxygenated hemoglobin (Hb) concentration using the modified Beer-Lambert law [25]. In order to remove the high frequency noise due to respiration and heartbeat, the signals were low-pass filtered using a 3^{rd}-order Butterworth filter of cut-off

frequency 0.2Hz. In this study, the averaged oxygenated hemoglobin (HBO) signal for each task over each run was considered for classification. The nirsLAB (v2014.05 by NITRC) was used to preprocess the NIRS measurements. A total of 200 segments of 10 s were associated for each task.

The same process was performed for tEEG data. Each run was decomposed into segments of 10 s corresponding to each task (left, right, up and down) and rest. The average of these tasks over each run was calculated. Thus, for each subject there are a total of 80 segments of 10 s corresponding to each of the four tasks and for rest for the 8 electrodes used to record the tEEG signals. The tEEG segments were filtered using an 8^{th} order low pass Butterworth filter with 30 Hz cut-off frequency.

3.2.4 Motor Imagery Detection based on tEEG and NIRS System

The aim of BCI is to translate the brain activities into commands for a special device such as computer. To achieve this goal, classification algorithms can be used. In this paper, an offline classification of the tEEG and NIRS signals recorded during motor task imagery were performed. The classification accuracy depends on both the features and the classification algorithm used. These two steps are highlighted in this section.

3.2.4.1 Feature Extraction

As already mentioned in the above section, the duration of each task is 10 s. To improve the classification accuracy, the window sizes (1s, 2s, 3s 4s and 5s) were tested for feature extraction. One second sliding Hamming window was adopted since

it gives the best accuracy among all the tested window sizes from both tEEG and NIRS. Then the signal mean and the signal median (MAD) for each one second segment were computed. For the dataset: $X = x(1), x(2), ..., x(N)$, the MAD is defined as the median of the absolute deviations from the data's median [26]:

$$MAD = median(|X - median(X)|) \tag{3.1}$$

Therefore, for each 10 s segment, there were 10 two dimensional data points for mean and median values of windowed segments. For NIRS data the feature vector was calculated from 200 segments of 10 s each for each task (20 channels for 10 runs). For tEEG data, the feature vector was calculated from 80 segments of 10 s each for each task (8 electrodes for 10 runs).

3.2.4.2 Classification

The classification was performed using two different classifiers, the support vector machine (SVM) [27] classifier and the k-nearest neighbor (k-NN) [28] classifier.

3.2.4.2.1 Support Vector Machine (SVM)

The SVM classifier developed by V. Vapnik [27] has shown to perform well in real world problems, including BCI. The idea of SVM is to separate the data $x \in R^n$ into two classes by finding a weight vector $w \in R^n$ and an offset $b \in R$ of a hyperplane H:

$$\begin{aligned} H &: R^n \rightarrow \{-1, 1\} \\ x &\rightarrow sign(w \times x + b) \end{aligned} \tag{3.2}$$

The classification is done by constructing an n-dimensional hyper-plane that optimally

separates the data into two categories by maximizing the distance from the decision boundary to the nearest data-points (called support vectors) in the training data. In this study, we generate non-linear decision boundaries using Gaussian radial basis function (RBF) kernel [29]. This kernel was selected due to the highest classification results obtained were better when compared to other SVM kernels (linear, quadratic, polynomial) that were tested.

3.2.4.2.2 k-Nearest Neighbor (k-NN)

k-NN is a non-parametric and nonlinear classifier suitable for n-dimensional, multi-modal problems [28]. The k-NN approach has recently been recognized as a very important algorithm, due to its high classification accuracy in problems with unknown and abnormal distributions [28]. The k-NN classification finds a group of k objects in the training set that are closest to the test object, and assigns a label on the predominance of a particular class in this neighborhood [28]. Using the k-NN classifier, three important components must be identified: a set of labeled objects, a distance or similarity metric to compute distance between objects, and the value of k, the number of nearest neighbors. In this paper, the linear distance measure was selected and the number of nearest neighbor k was set to be one, which provided highest detection accuracy when compared to other values of k (k=2, 3, 4,..).

3.2.4.3 Data Training and Performance Measurement

The classification is based on two separate sets of training and testing data containing the extracted feature from each task. In this study, we performed a ten-fold

cross-validation to determine the classification accuracy. In ten-fold cross validation, the data set is split into 10 equal sub-set partitions. In each iteration, one of the 10 subsets is used for testing whereas the other 9 subsets are used for training the dataset. The total data were randomly split into ten subsets. The whole procedure is repeated ten times. The final result is the average of all 10 repetitions. One important advantage of the cross-validation technique is the avoidance of the over-fitting problem [32].

In order to evaluate the performance of the proposed algorithm for imagery task classification, accuracy was calculated as follows [30]:

$$\text{Accuracy (Acc)} = \frac{\text{TP} + \text{TN}}{\text{TP} + \text{TN} + \text{FP} + \text{FN}} \tag{3.3}$$

where TP, TN, FN, and FP represent the numbers of true positive, true negative, false negative, and false positive, respectively.

3.2.4.4 Online tEEG Control of Cursor Movement

In this part, we conducted an online experiment involving all 9 subjects. The subjects performed one session of feedback training to perform a two dimensional cursor control using their motor imagery. The tEEG recording methods and processing in BCI2000 were the same as in the offline analysis. The signal was recorded from the same 8 locations (C3, C1, Cz, C2, C4, FC1, FCz, FC2) using the TCREs according to the international 10-20 system.

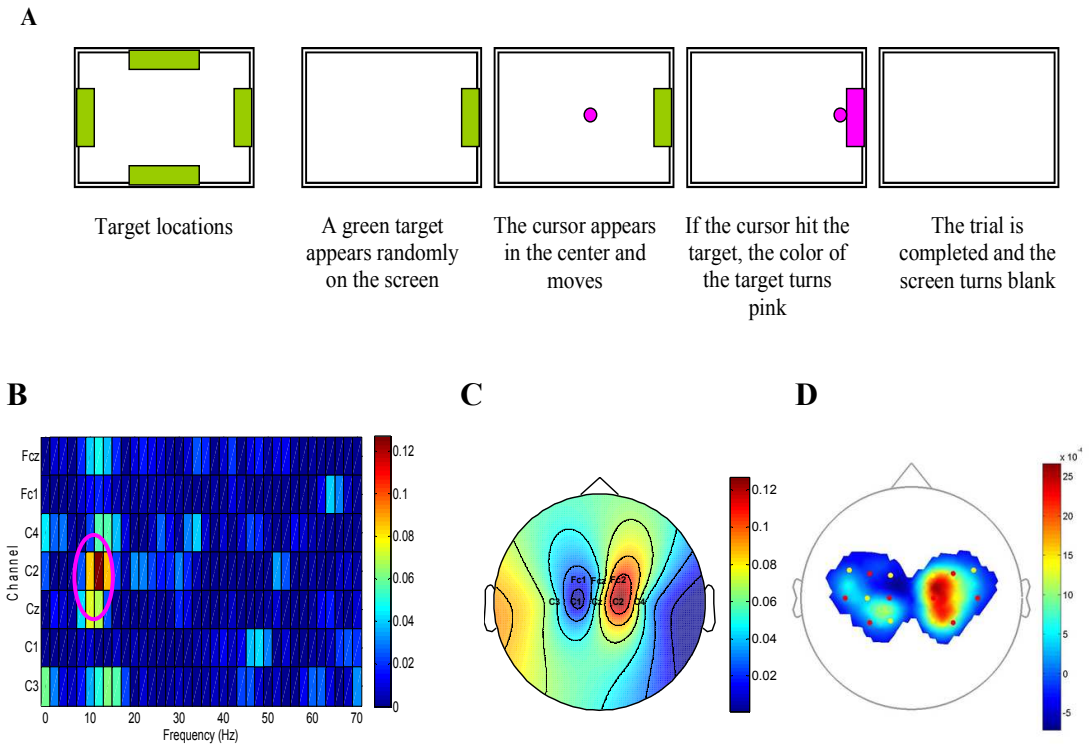

Figure 3.4 (A) the sequence of event for a trial from the appearance of a target to the end of a trial. (B) Values of r^2 between imagined left movement and rest for Subject 1, (C) Topographical properties of subject 1, (D)Topography mapping of oxygenated hemoglobin (HbO_2) for subject 1.

The subject was asked to move a computer cursor from the center of the screen and hit a target that appeared in one of four locations of the screen: up, down, right, or left. Subjects imagined moving their right hand to move the cursor to the right, their left hand to go left, both hands for up, and both feet for down. The trial sequence used for two-dimensional cursor movement is shown in Figure 3.4-A. The target appeared in one of the four possible locations on the sides of the screen. Then a cursor, in the form of small ball, appeared at the center of the screen. The ball was free to move in two dimensions and is controlled by the subject's mental imagery recorded by tEEG or NIRS. When the ball reached the target, the target changed color. After that, the screen

went blank and then the next trial began. If the subject failed to hit the target within 10 s, the target disappeared and the trial was considered as a failed trial. Each of the nine subjects has one session of five runs (20 trials per run) to performs the two dimensional cursor control.

The tEEG features used for online control of cursor movement are the amplitudes at particular frequency bands at certain electrode locations that have larger amplitude changes corresponding to the related task. These amplitudes were computed by calculating the coefficient of determination r^2 [31]. The values of r^2 show how much control the subject had over each particular frequency and electrode location for the corresponding task. Figure 3.4-B shows an example of r^2 values of subject 1 for left versus rest task.

3.3 Results and Discussion

The objective of this study was to detect four different imagery tasks using two different modes of BCI: (1) Laplacian EEG (tEEG) based BCI and (2) NIRS signal based BCI. The proposed method has successfully demonstrated the capability of distinguishing the four imagery tasks, left, right, up and down using tEEG and NIRS based BCI. The results of the four imagery task classification using the averaged tEEG and the averaged NIRS data are shown in Table 3.1 and Table 3.2, respectively. Due to individual differences the classification accuracies varied by subjects. However, some of the subjects reached high accuracy. The individual offline classification accuracies ranged from 64.10% to 99.97% using the tEEG signals and from 57.12% to 87.26% using the NIRS signals.

Table 3.1 Offline classification accuracies, four different offline control commands were performed from each of the 9 subjects: left vs. rest, right vs. rest, up vs. rest and down vs. rest using the averaged ***tEEG*** signal.

	Left Vs. Rest (%)		**Right Vs. Rest (%)**		**Up Vs. Rest (%)**		**Down Vs. Rest (%)**	
	SVM	**k-NN**	**SVM**	**k-NN**	**SVM**	**k-NN**	**SVM**	**k-NN**
1	87.32	71.88	72.22	77.78	77.78	72.22	81.48	70.37
2	75.93	81.48	85.19	79.63	75.93	76.63	71.13	81.76
3	72.22	70.32	72.03	76.99	75.87	71.36	80.12	79.32
4	79.58	75.45	84.79	81.08	81.48	83.33	64.81	72.22
5	79.63	75.93	74.07	75.93	83.33	70.37	80.35	80.23
6	80.63	75.01	75.93	74.07	82.65	82.63	74.10	79.51
7	78.22	75.03	83.53	82.98	84.84	75.33	86.48	80.29
8	93.14	99.97	94.31	94.22	88.34	92.44	92.59	98.37
9	64.10	66.25	72.22	66.67	67.36	67.69	67.33	66.56
Average	78.97	76.81	79.36	78.81	79.73	76.88	78.88	78.73

Table 3.2 Offline classification accuracies, four different offline control commands were performed from each of the 9 subjects: left vs. rest, right vs. rest, up vs. rest and down vs. rest using the averaged ***NIRS*** signal.

	Left Vs. Rest (%)		**Right Vs. Rest (%)**		**Up Vs. Rest (%)**		**Down Vs. Rest (%)**	
	SVM	**k-NN**	**SVM**	**k-NN**	**SVM**	**k-NN**	**SVM**	**k-NN**
1	80.22	84.56	86.15	80.66	86.85	75.88	88.23	84.21
2	73.33	72.28	72.36	73.12	66.98	70.89	68.41	67.69
3	71.27	68.98	68.74	70.22	73.56	72.87	77.33	74.26
4	80.25	79.85	81.20	76.66	64.02	62.64	70.55	57.12
5	64.02	60.62	64.65	60.42	64.31	57.48	63.79	60.54
6	89.11	87.22	89.63	86.54	90.52	89.36	91.84	90.69
7	86.52	82.99	84.64	79.71	91.62	87.54	92.05	87.63
8	68.42	67.34	66.44	60.54	68.21	66.55	69.75	67.22
9	87.26	84.55	85.32	83.47	81.65	84.26	81.74	80.95
Average	77.82	76.48	77.68	74.59	76.41	74.16	77.74	74.47

Table 3.3 Offline classification accuracies, four different offline control commands were performed from each of the 9 subjects: left vs. rest, right vs. rest, up vs. rest and down vs. rest using the single events ***tEEG*** signal.

	Left Vs. Rest (%)		**Right Vs. Rest (%)**		**Up Vs. Rest (%)**		**Down Vs. Rest (%)**	
	SVM	**k-NN**	**SVM**	**k-NN**	**SVM**	**k-NN**	**SVM**	**k-NN**
1	61.57	63.66	56.82	56.82	62.5	63.64	60.42	62.88
2	57.58	63.45	66.48	62.69	65.85	65.53	58.35	61.95
3	68.18	70.08	70.84	73.93	72.17	68.15	67.8	61.36
4	67.98	68.93	67.15	69.49	64.02	66.67	62.88	68.75
5	60.23	66.67	58.33	61.74	58.14	66.67	61.45	68.86
6	57.66	59.85	60.8	57.77	63.79	58.41	62.52	59.35
7	68.75	70.27	65.72	70.83	66.67	73.3	66.67	70.64
8	78.36	92.27	73.32	88.79	84.49	90.25	75.21	90.02
9	55.65	57.23	50.65	54.33	62.12	65.88	58.92	55.33
Average	63.99	68.04	63.34	66.26	66.63	68.72	63.80	66.57

Table 3.4 Offline classification accuracies, four different offline control commands were performed from each of the 9 subjects: left vs. rest, right vs. rest, up vs. rest and down vs. rest using the single events ***NIRS*** signal.

	Left Vs. Rest (%)		**Right Vs. Rest (%)**		**Up Vs. Rest (%)**		**Down Vs. Rest (%)**	
	SVM	**k-NN**	**SVM**	**k-NN**	**SVM**	**k-NN**	**SVM**	**k-NN**
1	50.22	51.78	54.44	50.12	61.75	60.98	54.55	57.85
2	58.42	63.85	60.52	59.78	59.66	54.48	56.71	55.32
3	61.85	59.85	69.58	66.45	69.86	66.21	58.75	59.48
4	57.85	60.12	62.33	61.79	59.85	54.82	57.23	55.64
5	55.25	59.4	57.56	52.93	60.12	58.24	55.23	57.55
6	50.45	51.23	58.26	55.46	60.24	57.55	52.28	54.88
7	66.85	61.92	58.76	54.1	50.21	57.84	60.87	59.76
8	76.28	77.85	69.78	72.15	73.49	69.76	79.23	77.44
9	80.55	78.54	60.32	62.75	61.79	66.75	69.46	64.85
Average	61.96	62.72	61.28	59.50	61.88	60.73	60.47	60.30

The proposed method has successfully demonstrated the capability of distinguishing the four imagery tasks, left, right, up and down using tEEG and NIRS based BCI.

Considering the two types of classifiers used, k-NN and SVM, it was observed that both classifiers were successfully classifying the four tasks using tEEG and NIRS signals. Comparing the accuracies of the four tasks from Tables 3.1 and 3.2 we can observe that the subjects reached different accuracies for the same task using tEEG and NIRS. For example subject 8 had an accuracy of 99.97% controlling the left task using tEEG while using the NIRS signal the same subject only reached an accuracy of 67.34%. Subject 9 reached 89.11% controlling the left task from rest using the NIRS signal and reached just 80.63% using the tEEG signal.

The single event for tEEG and NIRS were also tested. The individual offline classification accuracies ranged from 50.65% to 92.27% using the tEEG signals and from 50.12% to 80.55% using the NIRS signals. Table 3.3 and Table 3.4 show the single events accuracies for tEEG and NIRS, respectively. Comparing the single event results to the average, it is clear that the accuracies are improved after averaging the data.

The average accuracies of k-NN and SVM classifiers for each task using the averaged tEEG and NIRS signals were shown in Figures 3.5 and 3.6, respectively. Most of the 9 subjects had experimental classification accuracies near 80% when using the tEEG signals. Moreover one subject, subject 8, reached 99% using the tEEG signal. The average accuracies of k-NN and SVM classifiers for each task during single events of tEEG and NIRS signals were shown in Figures 3.7 and 3.8, respectively. The paired t-test between the averaged accuracies from tEEG signals

shown in Figure 3.5 and the averaged accuracies from the NIRS signals shown in Figure 3.6 are significantly different (p= 0.0047) with tEEG having higher accuracies than NIRS. Furthermore, the paired t-test between the averaged single event accuracies from tEEG signals shown in Figure 3.7 and the averaged single event accuracies from the NIRS signals shown in Figure 3.8 are also significantly different (p= 0.0080). Figure 3.9 shows that the results are still significantly different after Bonferroni t-test correction.

In this study the subjects performed one session in the online target acquisition phase. The subjects were trained to move a cursor with their tEEG signals to hit targets that appeared randomly one at a time, left, right, top, or bottom. The subjects were given 10 initial runs which were used for offline analysis. Figure 3.4-B shows the values of r^2 corresponding to imagined left hand movement versus rest for subject 1 from the offline analysis. The pink ellipse shape shows that the subject used 10-12Hz amplitude to move the computer cursor to the target that appeared in the left side of the screen. Figure 3.4-C shows the scalp topographies of subject 1. Finally, figure 3.4-D shows the topography mapping of oxygenated hemoglobin (HbO_2) for subject 1 with the energy clearly focused on the right motor cortex area. The online accuracies for 2D computer cursor control were around 50% for most of the subjects. We believe that the performance of the subjects would gradually be improved by increasing the training time.

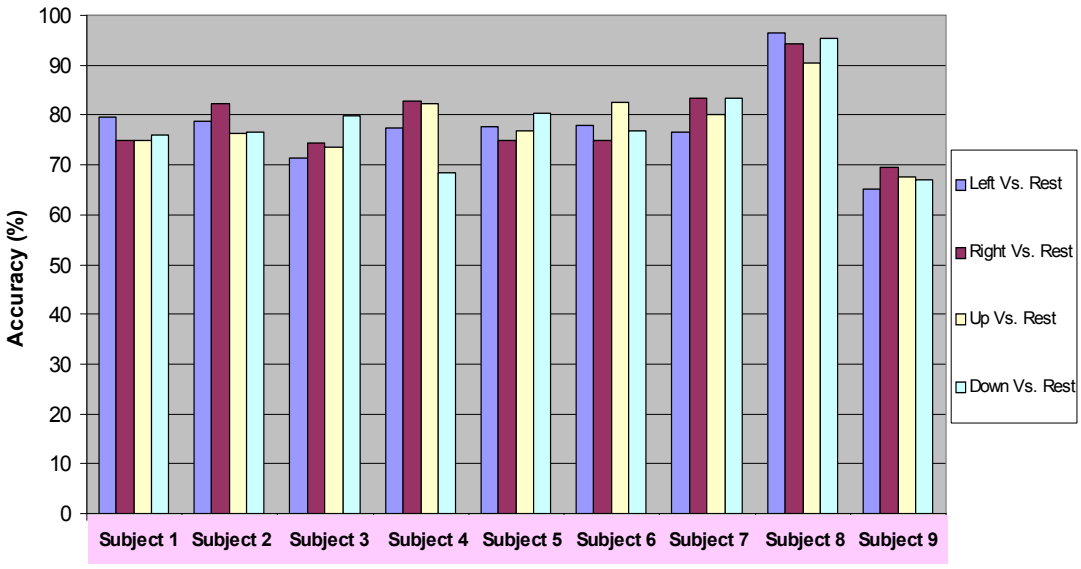

Figure 3.5 The average accuracy of k-NN and SVM of each offline task for each subject using the averaged tEEG signals.

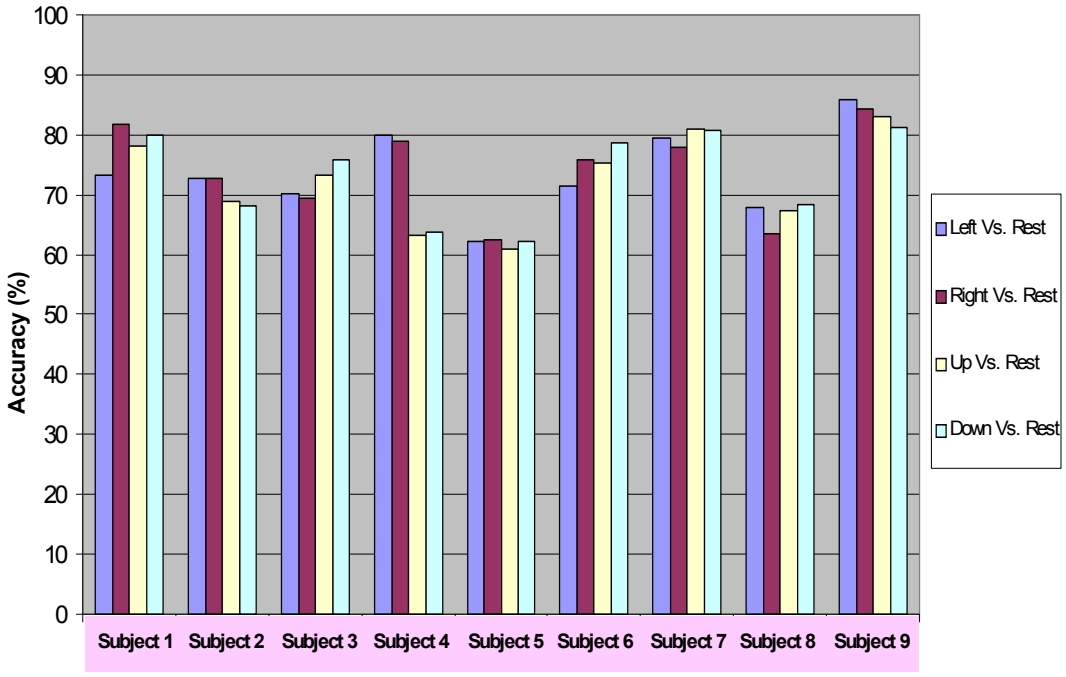

Figure 3.6 The average accuracy of k-NN and SVM of each offline task for each subject using the averaged NIRS signals.

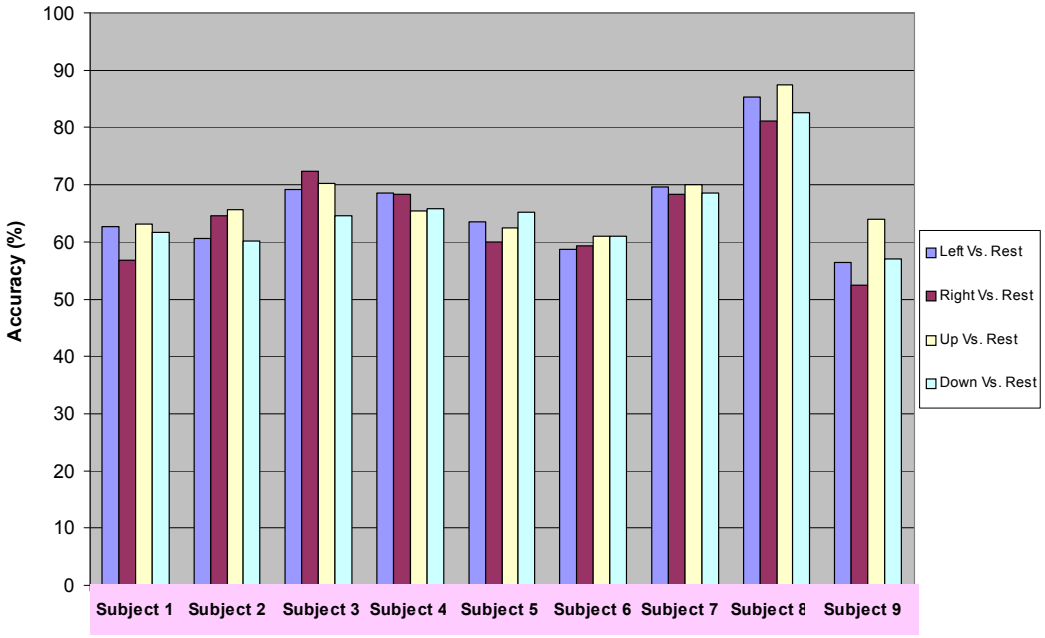

Figure 3.7 The average accuracy of k-NN and SVM of each offline task for each subject using the single event tEEG signals.

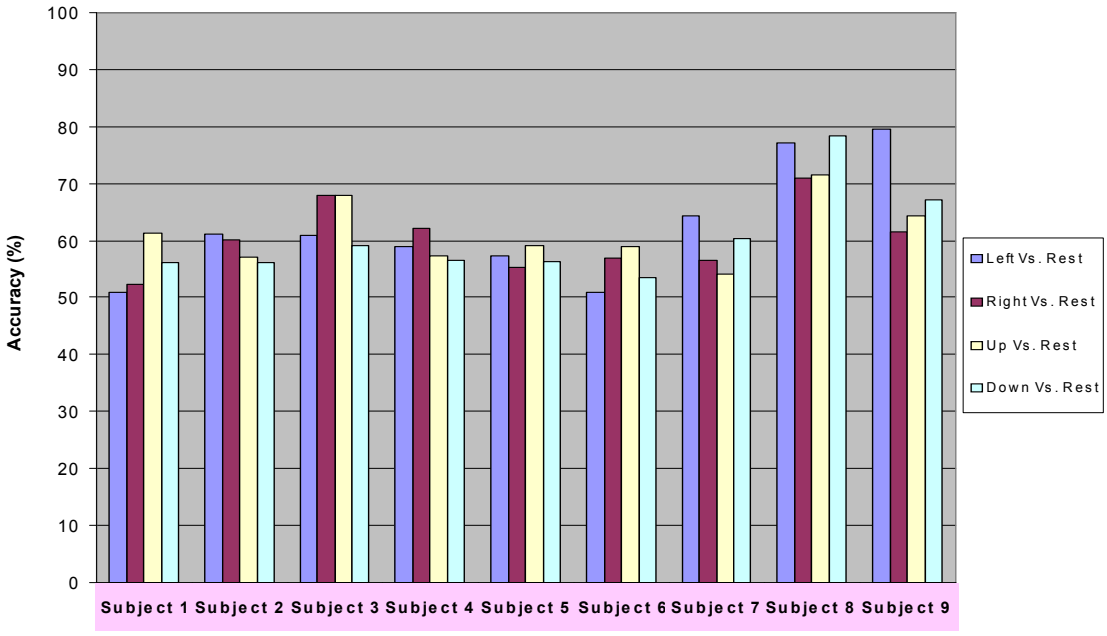

Figure 3.8 The average accuracy of k-NN and SVM of each offline task for each subject using the single event NIRS signals.

Table 3.5 Performance comparison

Reference	Sitaram et al. [18]	Al Zoubi et al. [30]	Lei et al. [17]	Besio et al. [22]		**The proposed method**	
Modality	NIRS	EEG	EEG	EEG, tEEG		tEEG, NIRS	
Number of Subjects	5	3	3	12		9	
Mental Tasks	Motor imagery (Left hand, Right hand)	Motor imagery (Left hand, Right hand, Foot , Tongue)	Motor imagery (Left hand, Right hand, Foot , Tongue)	Motor imagery (Left hand, Right hand)		Motor imagery (Left hand, Right hand, Both hands, Both feet)	
Period of training and testing	80 trials	Same day (240 trials)	Same day (360 trials)	(160-200 trials)		Same day (200 trials)	
Average/Single event data	Single event	Single event	Single event	Single event		Averaged and single event	
Max Accuracy (%)	75.62	93.89	68.08	73.34 (EEG)	84.23 (tEEG)	99.97 (averaged tEEG)	87.26 (averaged NIRS)
						92.27 (Single event tEEG)	80.55 (Single event NIRS)

As seen in Table 3.5, comparing our results to other studies using either tEEG or NIRS, the results from our proposed method achieved an improvement comparable to that of the others. The maximum accuracies achieved using the average tEEG signals and the averaged NIRS signals are 99.97% and 87.26%, respectively. However, the maximum accuracies achieved using single event tEEG signals and the single event NIRS signals are 92.27% and 80.55%, respectively. In the study of Sitaram et al. [18] the NIRS signal was used to accomplish motor imagery tasks. Sitaram et al. [18] used an SVM classifier to classify the left-hand imagery data from right-hand imagery data with a maximum accuracy of 75.62%. In the studies of Al Zoubi et al. [30] and Lei et

al [17], the process was based on the EEG signal; the data sets were recorded in the same day. Al Zoubi et al. used the dataset IIIa from the BCI III competition (6 runs with 40 trials each), the maximum accuracy reached from the tree subjects after a single event classification was 93.89%. In the previous work of Besio et al. [22], single event left/right hand motor imagery for EEG and tEEG signals were acquired and classified. The maximum accuracy from all the subjects was 84.23% for tEEG signal and 73.34% for the EEG signal. Their results also showed that TCREs (tEEG signal) generated significantly higher classification accuracy than disc electrodes (EEG signal).

One positive outcome of this study is that only one session for each subject was needed to accurately classify the four imagery tasks. Moreover, a simple set of features was used, the mean and the median, therefore it is expected that the processing could be performed in near real-time.

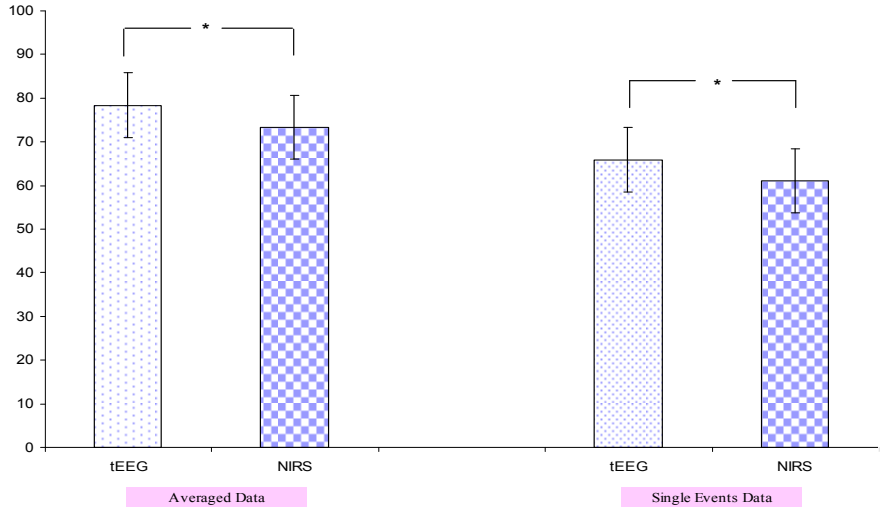

Figure 3.9 The average accuracies for all subjects from Figures 3.5 and 3.6 for averaged data and Figures 3.7 and 3.8 for single events data. Values are *mean* $\pm$ *SD* , *: $P < 0.01$.

Further research will be performed in the future by combining tEEG-NIRS features to evaluate the classification accuracy with a combined set of features. Moreover, it is recommended to test the method on subjects with significant motor impairment.

3.4 Conclusion

The present study addresses the usefulness of tEEG and NIRS based BCI for imagery task classification. The tripolar EEG and NIRS signals corresponding to left-hand motor imagery, right-hand motor imagery, both-hand motor imagery and both-feet motor imagery were acquired simultaneously from nine healthy subjects. The signal mean and signal median calculated during one second duration sliding time windows were used as the inputs to two different classifiers, SVM and k-NN, to evaluate the performance of the proposed method. The results demonstrated there was a significant difference in accuracy of 2D motor imagery with tEEG compared to NIRS-based BCI.

.

References

[1] J. R. Wolpaw, N. Birbaumer, W. J. Heetderks, D. J. McFarland, P. H. Peckham, G. Schalk, E. Donchin, L. A. Quatrano, C. J. Robinson, and T. M. Vaughan. "Brain-computer interface technology: a review of the first international meeting." *IEEE Transactions on Rehabilitation Engineering*, vol. 8, pp.164-173, 2000.

[2] F. Lotte, M. Congedo, A. Lécuyer and F. Lamarche. "A review of classification algorithms for EEG-based brain–computer interfaces," *Journal of Neural Engineering*, vol. 4, 2007.

[3] C. Neuper, G. R. Müller, A. Kübler, N. Birbaumer, and G. Pfurtscheller. "Clinical application of an EEG-based brain–computer interface: a case study in a patient with severe motor impairment." *Clinical Neurophysiology,* vol. 114, pp. 399-409, 2003.

[4] F. Lotte, M. Congedo, A. Lécuyer and F. Lamarche, "A review of classification algorithms for EEG-based brain–computer interfaces," *Journal of Neural Engineering*, vol. 4, 2007.

[5] J. Mellinger, G. Schalk, C.h Braun, H. Preissl, W. Rosenstiel, N. Birbaumer, and A. Kübler. "An MEG-based brain–computer interface (BCI)." Neuroimage 36, pp: 581-593, 2007.

[6] N. Weiskopf, R. Veit, M. Mathiak, W. Grodd, R. Goebel, N. Birbaumer, "Physiological self-regulation of regional brain activity using real-time functional magnetic resonance imaging (fMRI): methodology and exemplary data," *NeuroImage*, vol. 19, pp. 577-586, 2003.

[7] N. Weiskopf, M. Mathiak, S. W. Bock, F. Scharnowski, R. Veit, R. Goebel, N. Birbaumer, "Principals of a brain-computer interface (BCI) based on real-time functional magnetic resonance imaging (fMRI): methodology and exemplary data," *IEEE Transaction on Biomedical Engineering*, vol. 51, pp. 966-970, 2004.

[8] S. Coyle, T. Ward, C. Markham, and G. McDarby, "On the suitability of near-infrared (NIR) systems for next-generation brain–computer interfaces," *Physiological Measurement*, vol. 25, pp. 815-822, 2004.

[9] S. Ranganatha, H. Zhang, C. Guan, M. Thulasidas, Y. Hoshi, A. Ishikawa, K. Shimizu, and N. Birbaumer. "Temporal classification of multichannel near-infrared spectroscopy signals of motor imagery for developing a brain–computer interface," *NeuroImage*, vol. 34, pp. 1416-1427, 2007.

[10] K. Tai and T. Chau, “Single-trial classification of NIRS signals during emotional induction tasks: towards a corporeal machine interface,” *Journal of Neuroengineering and Rehabilitation*, vol.6, p.39, 2009.

[11] T. Ball, M. Mutscheler, A. Aertsen and A. Schulze-Bonhage, "Signal quality of simultaneously recorded invasive and non-invasive EEG," *NeuroImage*, vol. 46, pp. 708-716, 2009.

[12] W. Besio, K. Koka, R. Aakula, and W. Dai, “Tri-polar Concentric Ring Electrode Development for Laplacian Electroencephalography,” *IEEE Transactions on Biomedical Engineering*, BME, vol. 53, no. 5, pp. 926-933, 2006.

[13] K. Koka, W. Besio, “Improvement of spatial selectivity and decrease of mutual information of tri-polar concentric ring electrodes” *Journal of Neuroscience Methods*, vol. 165, pp. 216-222, 2007.

[14] Y. Boudria, A. Feltane, W. Besio, “Significant improvement in one-dimensional cursor control using Laplacian electroencephalography over electroencephalography,” *Journal of Neural Engineering*, vol. 11, 2014.

[15] S. M. Coyle, T. E. Ward and C. M. Markham, “Brain computer interface using a simplified functional near-infrared spectroscopy system,” *Journal of Neural Engineering*, vol. 3, pp. 219-226, 2007.

[16] N. Naser and S. K. Hong, “Classification of functional near-infrared spectroscopy signals corresponding to right and left wrist motor imagery for development of brain-computer interface,” *Neuroscience Letters*, vol. 553, pp. 84-89, 2013.

[17] X. Lei, P. Yang, and D. Yao, "An empirical Bayesian framework for brain–computer interfaces." *IEEE Transactions on Neural Systems and Rehabilitation Engineering*, vol. 17, pp. 521-529, 2009.

[18] R. Sitaram, H. Zhang, C. Guan, M. Thulasidas, Y. Hoshi, A Ishikawa and N. Birbaumer, “Temporal classification of multichannel near-infrared spectroscopy signals of motor imagery for developing a brain–computer interface,” *NeuroImage*, vol. 34, pp. 1416-1427, 2007.

[19] K. S. Hong, N. Naseer, and Y. H. Kim. "Classification of prefrontal and motor cortex signals for three-class fNIRS–BCI." *Neuroscience letters*, vol. 587, pp. 87-92, 2015.

[20] S. D. Power, T. H. Falk and T. Chau, “Classification of prefrontal activity due to mental arithmetic and music imagery using hidden Markov models and

frequency domain near-infrared spectroscopy," *Journal of Neural Engineering*, vol. 7, 026002, 2010.

[21] M. J. Khan, M. J. Hong and K. S. Hong," Decoding of four movement directions using hybrid NIRS-EEG brain-computer interface," *Frontiers in Human Neuroscienc*e, vol. 8, 2014.

[22] W. Besio, H. Cao, P. Zhou, "Application of Tripolar Concentric Electrodes and Pre-Feature Selection Algorithm for Brain-Computer Interface," *IEEE Transaction on Neural Systems & Rehabilitation Engineering*, vol. 16, pp. 191-194, 2008.

[23] R. W. Homan, J. Herman and P. Purdy, "Cerebral location of international 10-20 system electrode placement *Electroencephalography and Clinical Neurophysiology*, vol. 66, pp. 376-382, 1987.

[24] G. Schalk, G. D. J. McFarland, T. Hinterberger, N. W. Birbaumer and J. R. Wolpaw, "BCI2000: a general-purpose brain–computer interface (BCI) system," *IEEE Transaction of Biomedical Engineering*, vol. 51, pp. 1034–43, 2004.

[25] L. Koscis, P. Herman and A. Eke, "The modified Beer-Lambert law revisited," *Physics in Medicine and Biology*, vol. 51, n. 91, 2006.

[26] P. J. Rouss and C. Croux, "Alternatives to the median absolute deviation," *Journal of the American Statistical association*, vol. 88, pp.1273–1283, 1993.

[27] V. N. Vapnik, The Nature of Statistical Learning Theory, New York: Springer Science and Business Media, 2013.

[28] S. Zhang, "KNN-CF Approach: Incorporating Certainty Factor to k-NN Classification," *IEEE Intel Informatics Bulletin*, vol. 11, pp. 24-33, 2010.

[29] S. R. Gunn, "Support vector machines for classification and regression," Technical Report, University of SOUTHAMPTON, 1998.

[30] O. Al Zoubi, I. Koprinska and R. A. Calvo, "Classification of brain-computer interface data," *In Proceedings of the 7th Australasian Data Mining Conference, Australian Computer Society*, Inc., vol. 87, pp. 123-131, 2008.

[31] T. H. Wonnacott, R. Wonnacott, Introductory Statistics, vol. 3 edition. John Wiley and Sons; New York: 1977.

[32] S. Arlot, and A. Celisse, "A survey of cross-validation procedures for model selection," *Statistics Surveys*, vol. 4, pp. 40-79, 2010.

MANUSCRIPT 4

Phase Compensation of Tracking Control Using Delays of Feedback System

by

Yacine Boudria[1], Richard J. Vaccaro[1], Musa K. Jouaneh[2]

Published in The Mediterranean Journal of Measurement and Control, vol. 10, no.2, pp. 235-243, 2014

.

[1] Department of Electrical, Computer and Biomedical Engineering University of Rhode Island, Kingston, RI 02881, Email: yaciboud@gmail.com, vaccaro@ele.uri.edu.

[2] Department of Mechanical, Industrial and Systems Engineering University of Rhode Island, Kingston, RI 02881, Email: jouaneh@egr.uri.edu.

Abstract

This paper presents the design of a digital tracking control system for minimum phase plants, which results in a plant output that is a pure delay of the reference input. The tracking system consists of a feedback control system, which could be either a proportional integral derivative (PID) or state feedback with additional dynamics, and a feedforward inverse system. The inverse system can be designed using the zero phase error tracking control, which is denoted by ZPETC or by a state-space feedforward inverse filter, which we denote by FIF. The FIF equations are derived and, unlike ZPETC, can be evaluated even for a system with zeros inside the unit circle, located on the negative real axis, close to -1 and at z = 1. In both simulations and hardware experiments with a DC motor, the best tracking performance was achieved using a state feedback control with FIF. The proposed design procedure is simple and easy to implement.

4.1 Introduction

The objective of tracking control is to obtain a small path-following error for a given reference input or desired path. e.g., automated arc welding (certain trajectory) and servo turning table (uncertain trajectory). One way to achieve this is to design a stable feedback control system and then calculate a feedforward controller consisting of the inverse of this closed-loop system.

Early work on system inversion was done by Massey et al. [1] who stated the necessary and sufficient conditions for the existence of a feedforward linear inverse system. Vito et al. [2] has addressed the problem of designing a feedforward block of a

two degree of freedom controller for a discrete single input single output linear system with model uncertainty [3]. Fabrizio et al. [4] proposed a solution for the synthesis of a feedforward control action for a fractional control synthesis; this research has received a great attention from academia and industry because of the need to meet more stringent tracking system requirement.

Two types of architectures for inversion exist: plant inversion and closed-loop inversion. When the closed-loop system is non-minimum phase (i.e. has zeros outside the unit circle), the inverse system will be unstable. There are several partial solutions to this problem: the zero phase error tracking controller (ZPETC) [5, 6, 7, 8], the zero magnitude error tracking controller (ZMETC) [9, 10, 11], non-causal inverse [12, 13], the Truncated Series Approximation scheme (TSA) [14] and the non-causal Taylor series approximation [15].

ZPTEC was proposed in [8] and developed in [16, 17]. This algorithm is considered as one of the most successful feedforward controller designs and has attracted the attention of many researchers as an effective and simple method for approximately inverting non-minimum phase systems (e.g. [18, 19]). Using ZPETC, the poles that arise from inverting non-minimum phase zeros are approximated using stable poles and an appropriate gain factor; hence, the cascade of ZPETC and a given closed-loop system is approximately a pure delay. The use of an inverse system such as ZPETC allows the tracking system to follow time-varying reference inputs with small error. However, ZPETC has some shortcomings, such as gain errors and its inability to handle systems with a zero inside the unit circle, located on the negative real axis, close to -1 and at $z = 1$. This has motivated additional research [20-22].

Many applications related to this work, electro-hydraulic actuator [23, 24], NC machine tools [25], industrial motion control [26], ZPETC Path-Tracking gain-scheduling design and real-time multi-task flight simulation for the automatic transition of tilt-rotor aircraft [27], method for precise time synchronization based on FPGA [28] and so forth…

In this paper, we consider the above limitations of ZPTEC algorithm, and we introduce a state-space algorithm for computing the inverse of a given closed loop control system. We advocate the use of a feedforward system that inverts the closed-loop system model rather than the plant model. The reason is that the plant model is inaccurate while the modeling errors for the closed-loop system are reduced by the effects of feedback. The cascade of the inverse system, which we call the feedforward inverse filter (FIF), and the given closed-loop system, is a pure delay. Thus, the plant output will be an exact, delayed replica of the reference input. The proposed approach for computing the FIF works even when the plant has zeros arbitrarily close to the unit circle. Two inversion methods, ZPETC and FIF, will be used with two different closed-loop control systems: a proportional integral derivative (PID) controller and a standard state-space tracking system. The best results, in both simulations and hardware experiment, are obtained by combining FIF with the standard state-space tracking system.

The remainder of this paper is organized as follows; Section II introduces a standard PID controller, a standard state-space tracking system, as well as the algorithm for computing the FIF. Section III presents simulation and experimental

results, with a motor positioning system. Section IV contains conclusions and recommendations for future work.

4.2 Digital Closed-Loop system design

Consider an n^{th}-order single-input, single-output plant with state-space model:

$$\begin{aligned} \dot{x}(t) &= Ax(t) + Bu(t) \\ y(t) &= Cx(t) \end{aligned} \tag{4.1}$$

with $A \in R^{n\times n}$, $B \in R^{n\times 1}$ and $C \in R^{1\times n}$, where u(t) is the input of the system, y(t) the output and x(t) the state vector. In order to design a digital closed-loop control system for this plant, a discrete-time zero-order hold (ZOH) equivalent model that includes the effects of the D/A converter as well as the A/D converter sampling y(t) and x(t), is needed. The D/A and A/D converters operate with a sampling interval T seconds. The ZOH equivalent model is given by:

$$\begin{aligned} x[k+1] &= \Phi x[k] + \Gamma u[k] \\ y[k] &= Cx[k] \end{aligned} \tag{4.2}$$

with: $$\Phi = e^{AT} \quad \text{and} \quad \Gamma = \int_0^T e^{A\tau} B d\tau \tag{4.3}$$

4.2.1 PID controller system

A standard digital PID (proportional integral derivative) closed-loop system is shown in Figure 4.1. The digital PID equation is obtained using numerical integration of a continuous time PID equation, which shown below using Laplace transforms.

Notice that the derivative term is combined with a low-pass filter $\frac{N}{s+N}$ to limit its gain at high frequencies:

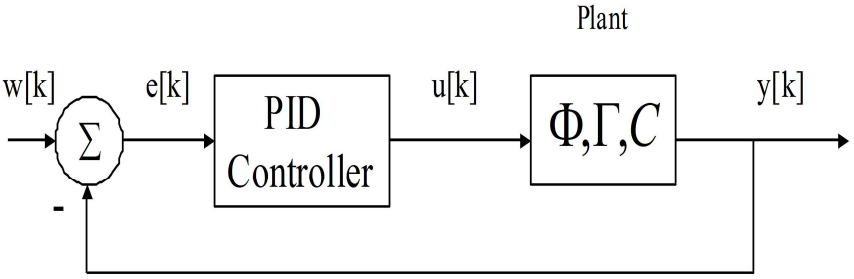

Figure 4.1 Closed-loop PID controller

$$U(s) = [K_P + \frac{K_I}{s} + K_D \frac{sN}{s+N}]E(s) \tag{4.4}$$

where N is the filter coefficient. The derivative term can be written in the form shown below:

$$\frac{K_D N}{1+\frac{1}{s}} E(s) \tag{4.5}$$

A discrete time approximation to (4.4) and (4.5) is obtained by replacing 1/s in the integral term by its backward Euler approximation $\frac{Tz}{z-1}$, and replacing 1/s in (4.5) by its forward Euler approximation $\frac{T}{z-1}$, where T is the sampling interval. The result is the following Z-transform equation:

$$U(z) = [K_P + K_I \frac{Tz}{z-1} + K_D \frac{N(z-1)}{z-1+NT}]E(z) \tag{4.6}$$

Letting x_1 be the state variable for the integral term and x_2 be the state variable for the derivative term, the following state-space model for the digital PID controller is obtained:

$$\begin{aligned} x_P[k+1] &= \Phi_P x[k] + \Gamma_P e[k] \\ y_P[k] &= C_P x[k] + D_P e[k] \end{aligned} \tag{4.7}$$

where, $$\Phi_P = \begin{bmatrix} 1 & 0 \\ 0 & 1-NT \end{bmatrix}, \Gamma_P = \begin{bmatrix} K_I T \\ -N^2 T K_D \end{bmatrix} \tag{4.8}$$

$C_P = [1 \quad 1]$, $\quad D_P = K_D N + K_I T + K_P$

The overall closed-loop system from $w[k]$ to $y[k]$ in Figure 4.1 is described by the following state-space model:

$$\begin{aligned} x_c[k+1] &= \Phi_c x_c[k] + \Gamma_c w[k] \\ y[k] &= C_c x_c[k] \end{aligned} \tag{4.9}$$

where, $$\Phi_c = \begin{bmatrix} \Phi - \Gamma D_P C & \Gamma C_P \\ -\Gamma_P C & \Phi_P \end{bmatrix}, \quad \Gamma_c = \begin{bmatrix} \Gamma D_P \\ \Gamma_P \end{bmatrix} C_c = [C \quad 0] \tag{4.10}$$

4.2.2 Digital state-feedback tracking system

In order to design a state-space feedback control system in which $y[k]$ tracks a class of reference inputs $w[k]$ with zero steady-state error one must use additional dynamics (see Figure 4.2).

$$x_a[k+1] = \Phi_a x[k] + \Gamma_a e[k] \tag{4.11}$$

Where the eigenvalues of Φ_a include the poles of the z-transform of $w[k]$ [15]. For the class of step inputs, only one eigenvalue is required at z = 1, which gives digital integral control. That is, for step input tracking, the additional dynamics are given by [29]:

$$\Phi_a = 1 \quad , \quad \Gamma_a = 1 \tag{4.12}$$

This tracking system will have zero steady-state error to a step input. Perfect tracking (with delay) may be achieved for a reference input $r[k]$ that is not a step signal by using an inverse system, FIF or ZPETC, between $r[k]$ and $w[k]$, as shown in Section III.

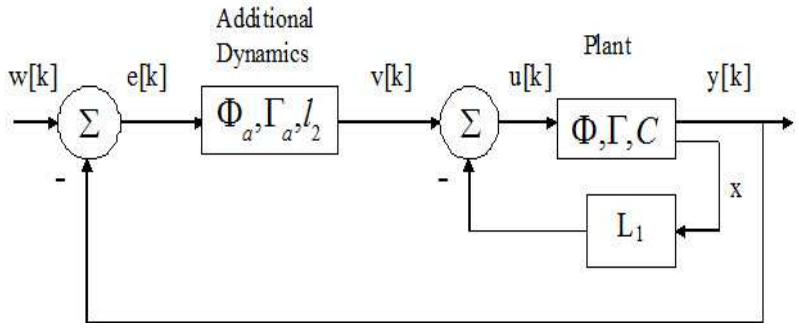

Figure 4.2 A standard state-space tracking system

In order to compute the $(1 \times n)$ state-feedback gain vector L_1 and the integrator gain l_2, a design model consisting of the cascade of the plant followed by the additional dynamics is needed. This design model is given by [29, 30]:

$$\overline{\Phi} = \begin{bmatrix} \Phi & 0 \\ \Gamma_a C & \Phi_a \end{bmatrix}, \qquad \overline{\Gamma} = \begin{bmatrix} \Gamma \\ 0 \end{bmatrix} \tag{4.13}$$

Given a desired vector of n+1 closed-loop poles, call it zpoles, a $1\times(n+1)$ gain vector $\overline{L}$ is computed (e.g. using the MATLAB place command) to obtain:

$$eig(\overline{\Phi} - \overline{\Gamma}\overline{L}) = zpoles \tag{4.14}$$

Then L_1 consists of the first n elements of $\overline{L}$ and l_2 is the last element of $\overline{L}$. The overall closed-loop system from $w[k]$ to $y[k]$ in Figure 4.2 is described by the following state-space model:

$$\begin{aligned} x_c[k+1] &= \Phi_c x_c[k] + \Gamma_c w[k] \\ y[k] &= C_c x_c[k] \end{aligned} \tag{4.15}$$

where, $x_c[k] = \begin{bmatrix} x[k] \\ x_a[k] \end{bmatrix}$, and $\Phi_c = \begin{bmatrix} \Phi - \Gamma L_1 & \Gamma l_2 \\ \Gamma_a C & \Phi_a \end{bmatrix}$

$$\Gamma_c = \begin{bmatrix} 0 \\ \Gamma_a \end{bmatrix}, \qquad \text{and} \qquad C_c = \begin{bmatrix} C & 0 \end{bmatrix} \tag{4.16}$$

In order to achieve perfect tracking for a suitably band limited reference input; the inverse of the system (Φ_c, Γ_c, C_c) must be computed. A state-space method, called feedforward inverse filter (FIF) is described next.

4.2.3 Feedforward inverse filter

This subsection shows how to find a state-space model $(\Phi_f, \Gamma_f, C_{f,} D_f)$, called a feedforwad inverse filter (FIF), such that the cascade of the FIF and (Φ_c, Γ_c, C_c) is a pure delay of d samples, where d is the relative degree of (Φ_c, Γ_c, C_c). The relative

degree of a system is the number of poles minus the number of zeros. Recall that (Φ_c, Γ_c, C_c) is a model for the system from $w[k]$ to $y[k]$ in Figure 4.2. The transfer function of this system is:

$$H(z) = C_c(zI - \Phi_c)^{-1}\Gamma_c = \frac{b(z)}{a(z)} \tag{4.17}$$

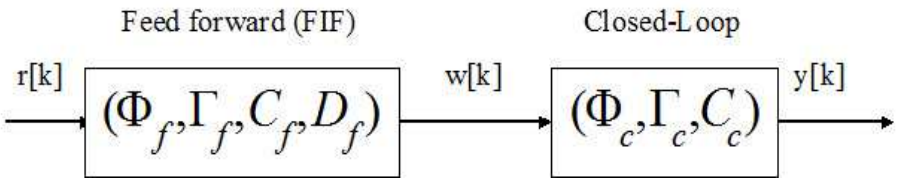

Figure 4.3 A closed-loop system in cascade with an FIF.

Let the degree of the numerator polynomial be called *m*, and the degree of the denominator polynomial *a(z)* be called *n*. A formal geometric series expansion for the matrix inverse in Equation (4.17) is:

$$(zI - \Phi_c)^{-1} = z^{-1}(I - z^{-1}\Phi_c)^{-1} \tag{4.18}$$

$$= z^{-1}[I + z^{-1}\Phi_c + z^{-2}\Phi_c^2 + \ldots]$$

Substituting Equation (4.18) into equation (4.17) yields:

$$\frac{b(z)}{a(z)} = z^{-1}C_c[I + z^{-1}\Phi_c + z^{-2}\Phi_c^2 + \ldots]\Gamma_c \quad = \sum_{k=1}^{\infty} C_c\Phi_c^{k-1}\Gamma_c z^{-k} \tag{4.19}$$

Dividing an m^{th} degree polynomial b(z) by an n^{th} degree polynomial *a(z)* yields a series in inverse powers of z with coefficients denoted by α_k. The first non-zero term in the series is the z^{m-n} term:

$$\frac{b(z)}{a(z)} = \sum_{k=n-m}^{\infty} \alpha_k z^{-k}, \quad \alpha_{n-m} \neq 0 \tag{4.20}$$

Comparing Equation (4.20) with equation (4.19) it can be seen that:

$C_c \Phi_c^{k-1} \Gamma_c = 0$, $k = 1,2,...,n-m-1$ and $C_c \Phi_c^{d-1} \Gamma_c \neq 0$, $d = n-m$

where d is the relative degree of the system, the number of poles minus the number of zeros. Once the FIF is calculated, it can be used in the overall system shown in Figure 4.3 to achieve perfect tracking with delay; that is, $y[k] = r[k-d]$. The FIF is derived by considering shifts of the outputs for the system shown in Equation (4.15), for example:

$$y[k+1] = C_c x_c[k+1] \quad = C_c \Phi_c x_c[k] + C_c \Gamma_c w[k] \tag{4.21}$$

If the relative degree of (Φ_c, Γ_c, C_c) is 1, then $C_c \Gamma_c \neq 0$. In general, the relative degree d is the smallest integer for which the coefficient of $w[k]$ is non-zero in the equation for $y[k+1]$. Assume that $d > 1$ so that $C_c \Gamma_c = 0$ then Equation (4.15) and equation (4.21) may be used to compute $y[k+2]$:

$$y[k+2] = C_c \Phi_c x_c[k+1] \; = C_c \Phi_c^2 x_c[k] + C_c \Phi_c \Gamma_c w[k] \tag{4.22}$$

If $d \geq 2$ then $C_c \Phi_c \Gamma_c = 0$ and $y[k+3]$ can be computed. This process is continued to get the following formula for $y[k+d]$.

$$y[k+d] = C_c \Phi_c^d x_c[k] + C_c \Phi_c^{d-1} \Gamma_c w[k] \tag{4.23}$$

The relative degree, d, is the smallest integer for which $C_c \Phi_c^{d-1} \Gamma_c$ is non-zero. Thus Equation (4.23) may be solved for $w[k]$ as follows: $w[k] = C_f x_c[k] + D_f y[k+d]$

where, $C_f = -(C_c \Phi_c^{d-1} \Gamma_c)^{-1} C_c \Phi_c^d$, $D_f = (C_c \Phi_c^{d-1} \Gamma_c)^{-1}$ (4.24)

The expression for $w[k]$ in Equation (4.24) is substituted into the state-update equation in Equation (4.15) to obtain:

Table 4.1 The design equations for feedforward inverse filter

---

1.Given (Φ_c, Γ_c, C_c) find the smallest integer d for which $C_c \Phi_c^{d-1} \Gamma_c$ is non-zero.

2.Compute the following:

$$D_f = (C_c \Phi_c^{d-1} \Gamma_c)^{-1}$$

$$C_f = -D_f C_c \Phi_c^d$$

$$\Gamma_f = \Gamma_c D_f$$

$$\Phi_f = \Phi_c + \Gamma_c C_f$$

3.The FIF is the state-space model $(\Phi_f, \Gamma_f, C_f, D_f)$ which, when cascade with (Φ_c, Γ_c, C_c) is equivalent to a pure delay of d samples.

$$x_c[k+1] = \Phi_f x_c[k] + \Gamma_f y[k+d] \quad \text{where,} \quad \Phi_f = \Phi_c + \Gamma_c C_f, \quad \Gamma_f = \Gamma_c D_f \qquad (4.25)$$

are a state-space model for a system whose input is $y[k+d]$ and output is $w[k]$. From Equation (4.15) we know that if $w[k]$ is the input to (Φ_c, Γ_c, C_c) the resulting output is $y[k]$. Thus, if $y[k+d]$ is the input to the cascade of $(\Phi_f, \Gamma_f, C_f, D_f)$ and (Φ_c, Γ_c, C_c), the output will be $y[k]$. Equivalently, if a reference input $r[k]$ is given to the cascade system, the output will be $y[k-d]$. Thus, the system shown in Figure 4.3 will achieve perfect tracking with a delay. A summary of the design equations for the FIF is given in Table 4.1.

Note that in order to achieve perfect tracking the magnitude of the frequency response of the FIF must be the reciprocal of the magnitude of the frequency response

of (Φ_c, Γ_c, C_c). A particular shaped reference input, shown in the next section, is used in this paper.

4.3 Simulation and experimental results

To illustrate the performances of the PID and the ADD control systems, with or without an inverse filter obtained from ZPETC or FIF, we considered the control of a single DC motor with encoder feedback. The motor is a Pitman DC-brush geared type motor with an incremental optical encoder (model GM9236C534-R2) and a gear ratio of 5.9:1. A 12 bit D/A converter, a pulse with modulator (PWM) servo amplifier (Model A12 from Advanced Motion Controls) and a data acquisition board (PCI-DAS-1002) are used for data conversion (A/D and D/A). The sampling interval is set to be 1 ms. In the following, we demonstrate the tracking control performance using the FIF algorithm with additional dynamics and compare it to PID controller, PID with FIF and ZPETC with FIF algorithms.

4.3.1 Open-Loop modeling process

A mathematical model for the first order motor system with velocity as the output signal was obtained from measured step response data for the actual motor system. Step inputs of different amplitudes were sent to the motor and the motor velocity was obtained by differentiating the measured angular position signal. Four different input voltage values (1V, 2V, 3V and 4V) were used and the resulting models were averaged to obtain the final model. This model gives numerical values for the motor parameters, shown in Table 4.2.

Table 4.2 Experimentally derived motor parameters

	Variable	Values
Viscous Friction	B	0.0094 *Nms*
Coulomb Torque	τ_c	0.0324 *Nm*
Inertia	J	1.12e^{-4} *Kgm*^{2}
Motor Constants	K_t	23e^{-3} *Nm/A*
	K_e	23e^{-3} *s/red*
	R	0.71 Ω

In Table 4.2, we also included a coulomb friction torque estimate for this system, where the friction torque is given by Equation (4.26).

$$\tau_f = Bw + sign(w)\tau_c \tag{4.26}$$

The non-linear friction was included in the simulation results that follow, and is present in the hardware system. However, only the linear system model, which ignored the Coulomb friction, was used to design the control systems. This linear system model, using the numbers in Table 4.2 is a state-space model as shown in Equation (4.1) with:

$$A = \begin{bmatrix} 0 & 1 \\ 0 & -84.2931 \end{bmatrix}, \quad B = \begin{bmatrix} 0 \\ 772.0482 \end{bmatrix}, \qquad C = \begin{bmatrix} 1 & 0 \end{bmatrix} \tag{4.27}$$

with: T=0.001s, the resulting ZOH equivalent:

$$\Phi = \begin{bmatrix} 1 & 0.001 \\ 0 & 0.9192 \end{bmatrix}, \quad \Gamma = \begin{bmatrix} 0.0004 \\ 0.7404 \end{bmatrix} \tag{4.28}$$

For model verification, we apply a sine wave to the hardware to obtain the experimental frequency response as shown in Figure 4.4.

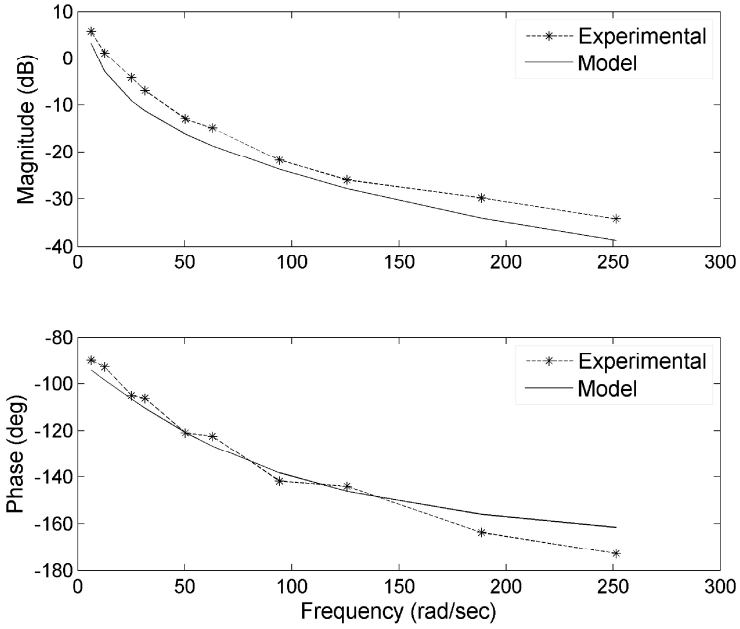

Figure 4.4 Frequency responses of experimental system and its model.

4.3.2 Closed-Loop tracking systems

After obtaining a model for the plant, the next step is to design a stable closed-loop system. We consider two different control systems, PID and ADD, shown in Figure 4.1 and Figure 4.2, respectively. These systems were designed to achieve a settling time of about T_s= 0:06s with adequate stability margins. For ADD, three desired closed-loop poles must be selected, and the L_1 and l_2 gains calculated. The closed-loop poles were chosen to be the roots of a normalized 1-second settling time 3rd order Bessel polynomial, scaled to achieve the desired settling time, and mapped into the z-plane. The normalized roots are [29]:

$$s_3 = [-5.0093, -3.9668 \pm 3.7845i] \tag{4.29}$$

Then the desired discrete time poles used in (4.14) are:

$$zpoles = e^{(\frac{Ts_3}{Ts})} \tag{4.30}$$

The resulting gains are L_1== [215.5012 0.7064], and l_2 = 19.7779

An experimental frequency response of the closed-loop ADD system is shown in Figure 4.5. The plant model used to generate Figure 4.5 is the same plant model used in Figure 4.4. However, the modeling error in Figure 4.5 is much less than that in Figure 4.4. That is, the model for the closed-loop system is much more accurate than the model for the plant itself. This is the motivation for using the FIF to invert the closed-loop system rather than the plant.

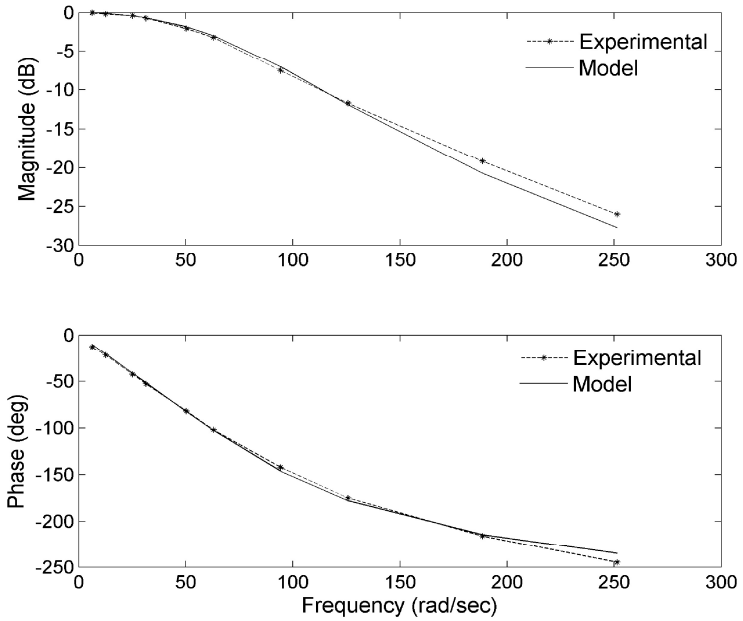

Figure 4.5 Frequency responses of experimental closed-loop ADD system and its model.

For the PID controller, the gains were adjusted by trial and error to obtain closed-loop poles close to those given by Equation (4.30). The resulting gains: $K_P = 30$, $K_I = 0.01$, $K_D = 0.3$, $N = 100$. The coefficient N (see Equation (4.4)) is chosen to give a bandwidth of about 16Hz for the low-pass filter, which was found to adequately limit the derivative noise in the hardware system.

Table 4.3 Zeros, Relative degree, Gain margin and Phase margin of the PID and ADD controllers' closed-loop

	PID Controller	ADD Controller
Closed-Loop zeros	-0.9723;0.95; 0.9999	-0.9723
Closed-Loop poles	0.9224+0.2003i 0.9224-0.2003i 0.9519; 0.9999	0.9342+0.0590i 0.9342-0.0590i 0.9199
Relative Degree (d)	1	2
Gain Margin	15.44 dB	23.93 dB
Phase Margin	31 degrees	69 degrees

The poles and zeros of the closed-loop PID and ADD systems and the corresponding stability margins are shown in Table 4.3.

4.3.3 Shaped input

When an inverse system such as ZPETC or FIF is used in conjunction with a closed-loop control system such as PID or ADD, the reference must be suitably band limited to prevent the inverse system from generating an excessively large output that would saturate the input to the hardware plant. In this paper, we calculate a shaped input signal by starting with the following sinusoidal acceleration signal, with amplitude A rad/s^2 and period D seconds:

$$a(t) = A\sin(2\pi \times t / D) \tag{4.31}$$

This equation may be integrated twice to obtain velocity and position signals, respectively. The constants of integration are chosen to make the initial values of velocity and position both zero. The resulting position signal is:

$$r(t) = \frac{AD}{2\pi}(t - \frac{D}{2\pi}\sin(2\pi \times t / D)) \tag{4.32}$$

In order to obtain a position of 1 radian at $t = D$ seconds, the following relationship between A and D must be satisfied:

$$A = \frac{2\pi}{D^2} \tag{4.33}$$

The reference input $w(t)$ is the concatenation of $r(t)$ at different times.

$$w(t) = \begin{cases} 0, & t < 0 \\ r(t), & 0 \le t < 2 \times D \\ -r(t) + 4 \times H, & 2 \times D < t \le 4 \times D \end{cases}$$

where, H is the amplitude of $r(t)$.

In what follows, we show results for $4D$ = 0:2 seconds. Figure 6 shows the simulated and experimental output for the PID controller without any inverse system. There is a significant phase lag for the PID controller and similarly for the ADD controller. However, the phase lag is eliminated from both controllers by using an inverse system, as shown next.

4.3.4 Inverse systems

In principal, either ZPETC or FIF could be used to obtain the inverse system for the PID or ADD control systems. However, as shown previously in Table 4.3, the PID control system has a pole-zero cancelation at z = 0.9999. If the PID system is given to the ZPETC as is, the ZPETC algorithm fails due to the zero location at z = 0.9999. In order to use ZPETC for the PID system one would have to give it the reduced-order model obtained by cancelling the pole and zero near 1. The FIF algorithm works with the given PID system as is. Note, that when the ADD has a zero at z = -0.9723, the ZPETC algorithm fails when a zero is located inside the unit circle, laying on the negative real axis and close to -1. As mentioned before, this behavior is documented in [1] and was confirmed in our study. For this reason the zero located at z = -0.9723, after inversion, will be considered as non stable pole. However, the FIF work as is.

In order to see the need for the FIF, the closed-loop PID system is used by itself to track a reference input that has two start-stop segments in the positive direction followed by two start-stop segments in the negative direction. The reference input has 95% of its energy in the frequency range from 0 to 5.5 Hz. The tracking results are shown in Figure 4.6, and it is clear that the closed-loop system has significant phase lag. Similar results are obtained with the ADD closed-loop system. The FIF may be used with either the PID or ADD closed-loop systems to eliminate the phase lag. Figure 4.7 and Figure 4.9 show the tracking results with the PID+FIF and ADD+FIF control system. Figure 4.8 shows Tracking performance of closed-loop ADD with ZPETC. Figure 4.10 shows the tracking errors for the PID system, as well as for the PID+FIF, ADD+ZPETC and ADD+FIF systems. It can be seen that the FIF with

either the PID or ADD closed-loop systems provides nearly perfect tracking of the reference input. Now suppose the reference input were scaled to a shorter duration, thus increasing its frequency content. Could the hardware system track this faster reference input? An answer to this question is found in Figure 4.11, which shows the plant-input voltages for the various tracking systems with the original reference input. The peak plant-input is about 6 volts, and the hardware has a 10-volt limit. Thus, the reference input used is within a factor of two of the tracking capability of the hardware.

Due to nonlinearities in the hardware system (e.g. nonlinear friction), the response to a reference input is not exactly repeatable. For this reason, we use a periodic reference input consisting of ten periods with a total duration of 2 second. The average squared error over the ten periods was computed as follows:

$$E = [\int_0^2 e^2(t)dt]/10 \tag{4.34}$$

The maximum absolute value of the error over the 2 second duration was also recorded. The values of these error measures for the various tracking systems are shown in Table 4.4.

Table 4.4 Tracking errors for periodic shaped input

	PID	PID+FIF	ADD+ZPETC	ADD+FIF
E (rad^2)	0.0930	0.0030	$2.429e^{-5}$	$1.9196e^{-5}$
Max|E (*rad*)|	0.0372	0.0076	0.0011	0.0009

4.4 Conclusion

A digital tracking control system for minimum-phase plants is presented in this paper. This controller is developed to reduce the phase lag caused by the feedback controller during the tracking control. The control system consists of two parts: a feedback control loop and a feedforward inverse system. For the feedback loop we used either a standard PID loop or a state-space tracking system with additional dynamics, which we denote by ADD. For the feedforward system we used either the ZPETC filter or a feedforward inverse filter, which we denote FIF. The FIF is calculated using the state-space formula shown in Table 4.1.

The main result in this paper is the state-space formula for the FIF. Because the FIF is outside of the feedback loop, it does not affect the stability of the closed-loop system or its robustness to modeling errors or disturbances. These depend only on the feedback loop. In this paper, the standard state-space and PID feedback loops both had good stability robustness as indicated by the gain and phase margins shown in Table 4.3.

As with any inverse method, one must question the robustness of the tracking error with respect to plant modeling errors. There will be errors in the model of any physical system, as shown for example in Figure 4.4. However, the model for the closed-loop system will be a much more accurate representation of the actual hardware due to the effect of feedback. For example, compare Figure 4.5 with Figure 4.4. The model of the closed-loop system in Figure 4.5 matches the hardware measurements almost exactly up to 100 rad/sec or about 16 Hz. The FIF for this system would be expected to provide nearly perfect tracking of any shape input whose frequency content was below

16 Hz. This precision-tracking bandwidth is much greater than could be obtained by feedback alone, and is needed for advanced motion-control applications.

In both simulations and experimental results with a DC motor system, the best tracking performance was achieved by ADD+FIF in reducing phase and gain error. Although, this paper considers only single-input, single-output systems, the FIF formulas in Table 4.1 are valid for minimum phase multi-input, multi-output systems. For minimum phase systems, the cascade connections of FIF with a feedback control loop is a pure time delay of d samples, where d is the relative degree of the plant. It remains for future work to develop formulas for FIF for a non-minimum phase plant. In this case it is not possible to achieve an overall system that is a pure time delay, and the goal will be to achieve an approximate time delay over as large a bandwidth as possible.

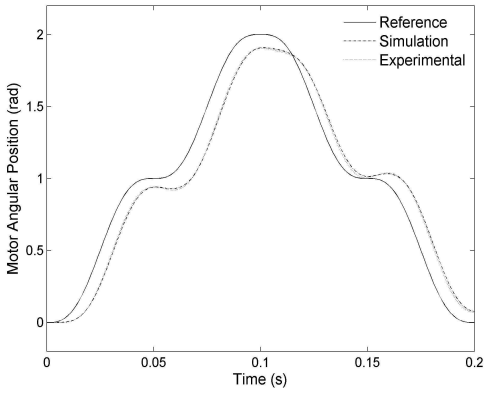

Figure 4.6 Tracking performance of closed-loop PID system.

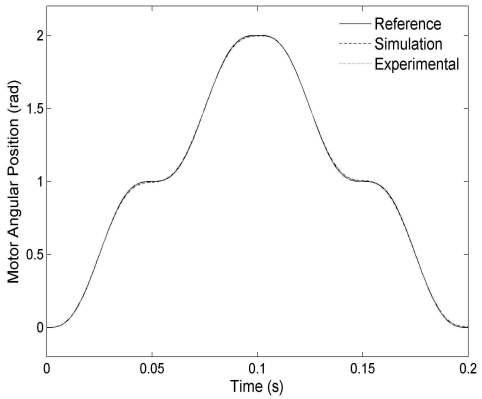

Figure 4.9 Tracking performance of closed-loop ADD with FIF.

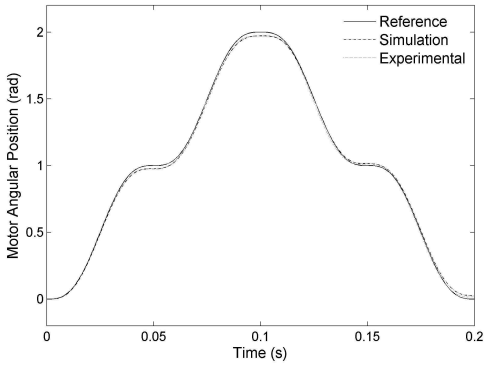

Figure 4.7 Tracking performance of closed-loop PID with FIF.

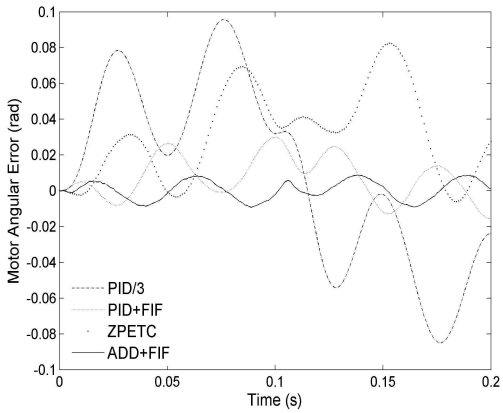

Figure 4.10 Experimental tracking error for the PID with FIF, ADD, ZPETC and ADD with FIF system.

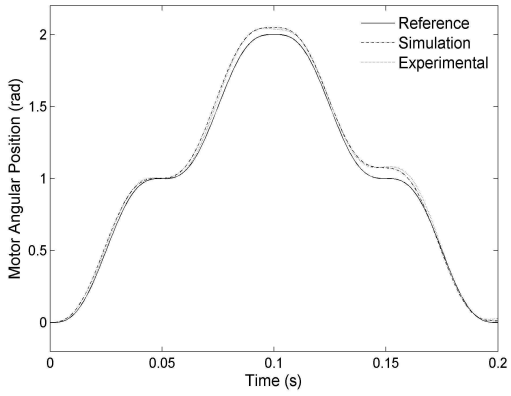

Figure 4.8 Tracking performance of closed-loop ADD with ZPETC.

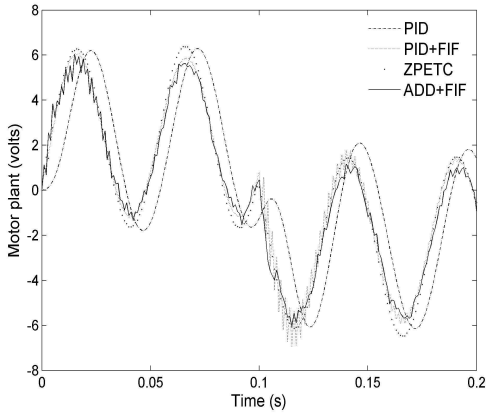

Figure 4.11 Experimental plant input voltages for PID, PID with FIF, ADD with ZPETC and ADD with FIF system.

References

[1] J. L. Massey, M. K. Sain, ”Inverse of linear sequential circuits,” *IEEE Transaction on Computers,* vol. C-17, pp. 330-337, 1968.

[2] C. Vito, M. Milanese, D. Regruto, “Robust feedforward design for a two-degree of freedom controller,” *Systems and Control Letters*, vol. 56, pp. 736-741, 2007.

[3] F. Padula, A. Visioli, “Inversion-based feedforward design for constrained fractional control systems,” *Proceeding of the European control conference, Zurich, CH*, pp. 4003–4008, 2013.

[4] P. Fabrizio, A. Visioli, “Inversion-based feedforward and reference signal design for fractional constrained control systems,” *Automatica*, vol. 50, pp. 2169-2178, 2014.

[5] P. M. Jackson, N. Ishak, R. Adnan, “Contouring Control of Non-Minimum Phase XY Table System using Trajectory ZPETC,” *International Journal of Scientific and Technology Research (IJSTR)*, vol. 6, pp. 80-85, 2012.

[6] E. D. Tung, M. Tomizuka, “Feedforward tracking controller design based on the identification of low frequency dynamics,” *Journal of Dynamic Systems, Measurement and Control*, vol. 115, pp. 348-356, 1993.

[7] M. Tomizuka, “Zero phase error tracking algorithm for digital control,” *Journal of Dynamic Systems, Measurement and Control (ASME)*, vol. 109, pp. 65-68, 1987.

[8] D. Torfs, J. De Schutter, and J. Swevers, "Extended bandwidth zero phase error tracking control of nonminimal phase systems," *Journal of dynamic systems, measurement, and control*, vol. 114, no.3,pp. 347-351, 1992.

[9] J. Wen, B. Potsaid, “An experimental study of a high performance motion control system”, *Proceeding of the American Control Conference, Boston, MA, USA*, pp. 5158-5163, 2004.

[10] K. Astrom, T. Hagglund, “Feedforward design”, *in Advanced PID Control Research triangle Park, NC: The Instrumentation, Systems and Automatica Society*, pp. 139-157, 2005.

[11] J. A. Butterworth, L. Y. Pao, D. Y. Abramovitch, “Analysis and comparison of three discrete-time feedforward model-inverse control techniques for nonminimum-phase systems,” *Mechatronics*, vol. 22, pp. 577-587, 2012.

[12] L. Silverman, "Inversion of multivariable linear systems", *IEEE Transaction on Automatic Control*, vol. 14, pp. 270-279, 1969.

[13] E. Bayo, H. Moulin, "An efficient computation of the inverse dynamic of flexible manipulators in the time domain", *Proceeding IEEE Robotics and Automatic Conference, Scottsadale, AZ*, pp. 710-715, 1989.

[14] E. Gross, M. Tomizuka, "Experimental exible beam time tracking control with a truncated series approximation to non cancelable inverse dynamics," *IEEE Transactions on Control Systems Technology*, vol. 2, pp. 382-391, 1994.

[15] B. Figney, L. Pao, D. Lawrence, "Nonminimum phase dynamic inversion for settle time applications", *IEEE Transaction on Control Systems Technology*, vol. 17, pp. 989-1005, 2009.

[16] Y. F. M. Yamada, S. Fujiwara, "Zero phase error tracking system with arbitrary specified gain characteristics", *Journal of Dynamic Systems, Measurement, and Control (ASME),* vol. 119, pp. 260-264, 1997.

[17] Y. F. M. Yamada, Z. Riadh, "Generalized optimal zero phase error tracking controller design", *Journal of Dynamic Systems, Measurement, and Control (ASME)*, vol. 121, pp. 165-170, 1999.

[18] L. J. Huang, M. Tomizuka, "A self paced fuzzy tracking controller for two-dimensional motion control", IEEE Transaction on Systems, Man and Cybernetics, vol. 20, pp. 1115-1123, 1990.

[19] Z. Jamaludine, H. V. Brussel, G. Pipleers, J. Swevers, "Accurate motion control of XY high-speed linear drivers friction model feed forward and cutting forces estimation", *Elsevier Journal on CIRP Annals - Manufacturing Technology*, vol. 57, pp. 401-406, 2008.

[20] B. Haack, M. Tomizuka, "The effect of adding zeroes to feed forward controllers", *Journal of Dynamic Systems, Measurement, and Control (ASME)*, vol. 113, pp. 6-10, 1991.

[21] H. S. Park, P. H. chang, D. Y. Lee, "Concurrent design of continuous zero phase error tracking controller and sinusoidal trajectory for improved tracking control", *Journal of Dynamic Systems, Measurement, and Control (ASME)*, vol. 123, pp. 127-129, 2001.

[22] H. S. Park, P. H. Chang, D. Y. Lee, "Continuous zero phase error tracking controller with gain error compensation", *Proceeding of the American Control Conference, San Diego, CA, USA*, vol. 5, pp. 3554-3558, 1999.

[23] N. Ishak, M. Tajjudin, H. Ismail, M. H. F. Rahiman, "Tracking control for electro-hydraulic actuator using ZPETC," *Proceeding of IEEE on Control and System Graduate Research Colloquium (ICSGRC), Shah Alam* , pp. 94-97, 2011.

[24] A. Ramli, A. M. Samad, M. M. Mustafa, "Real-time control of non-minimum phase electro-hydraulic system using trajectory-adaptive ZPETC," *7th International Colloquium on IEEE Signal Processing and its Applications (CSPA), Penang*, 2011, pp. 72-76, 2011.

[25] X. Zhao, Q. Guo, Y. Sun, "The Application of Optimal ZPETC in NC Machine Tool Servo Tracking Control [J]," *Modular Machine Tool & Automatic Manufacturing Technique*, vol. 4, 2005.

[26] M. Steinbuch, M. J. G. van de Molengraft, "Iterative learning control of industrial motion systems," *1st IFAC Conference on Mechatronic Systems, Darmstadt, Germany*, pp. 967-972, 2000.

[27] C. C. Peng, T. S. Hwang, S. W. Chen, C. Y. Chang, Y. C. Lin, Y. T. Wu, Y. J. Lin, W. R. Lai, "ZPETC Path-Tracking gain-scheduling design and real-time multi-task flight simulation for the automatic transition of tilt-rotor aircraft," *Proceeding of IEEE Robotics Automation and Mechatronics Conference*, pp. 118-123, 2010.

[28] W. J. Huang, B. Yu, "Method for precise time synchronization based on FPGA," *Journal Zhejiang University Engineering Science*, vol. 41, 2007.

[29] R. J. Vaccaro, Digital control: a state-space approach, McGraw-Hill, New York, NY, 1995.

[30] E. J. Davison, A. Goldenberg, "Robust control of a general servomechanism problem: the servo compensator", *Automatica*, vol. 11, pp. 461-471, 1975.

MANUSCRIPT 5

Inversion of MIMO Control Systems for Precision Tracking

by

Richard J. Vaccaro1, Yacine Boudria[1], Musa K. Jouaneh[2]

To be submitted to the American Control Conference.

[1] Department of Electrical, Computer and Biomedical Engineering University of Rhode Island, Kingston, RI 02881, Email: yaciboud@gmail.com, vaccaro@ele.uri.edu.

[2] Department of Mechanical, Industrial and Systems Engineering University of Rhode Island, Kingston, RI 02881, Email: jouaneh@egr.uri.edu.

Abstract

The problem considered is tracking control of a fully-coupled Multi-Input Multi-Output (MIMO) plant. We assume that a 2-degree-of-freedom feedback control system has been designed to get a stable closed-loop system having zero steady-state error to step inputs. Such a system has an inner feedback loop that stabilizes the plant. In order to have precision tracking for other types of inputs, some type of feedforward control is needed. The main contribution of this paper is an algorithm for calculating an inverse filter for the stabilized plant, which is an exact or approximate inverse for the closed-loop system. If the closed-loop system is minimum phase, the result is a decoupled system of delays. If the closed-loop system is non-minimum phase, the result is approximately a decoupled system of delays over a certain bandwidth. The calculation of the inverse filter and resulting tracking performance is demonstrated on an experimental belt-driven H-frame XY table, for which the system to be inverted is fully coupled and non-minimum phase.

5.1 Introduction

Feedforward filters from the reference signal to the plant input have been used to improve the performance of Single-Input Single-Output (SISO) tracking systems for many years. Typically, the feedforward filter is the inverse of the plant model. If the plant model is non-minimum phase the inverse model will be unstable, and some type of approximation is necessary. When the tracking system is implemented in discrete-time, non-minimum phase systems can be approximately inverted with some delay.

Methods for using feedforward filters in MIMO tracking systems are less well developed, especially for non-minimum phase systems. One recent contribution for MIMO systems is [1]. Instead of using one feedforward inverse system, two FIR blocks are used in a novel feedforward architecture. The resulting control system provides theoretically perfect tracking with delay. However, the development in [1] relies on the MIMO plant not being fully coupled in the sense that the method works only for plants having lower triangular transfer function matrices.

In this paper, we consider fully coupled MIMO systems and use a standard architecture in which there is a single feedforward filter from the reference signal to the plant input. We present a new method for approximately inverting a non-minimum phase stable MIMO system. The method may be used for plants that are not stable, provided a 2 degree-of-freedom control system is used which has an inner stabilizing feedback loop around the plant. There is a standard state-space tracking system architecture that has this required characteristic. The feedforward filter designed by the proposed approach approximately inverts the stable combination of the plant and inner feedback loop.

The outline of the paper is as follows. Section II reviews the development of a standard 2 degree-of freedom feedback (DoF) control system. Section III deals with MIMO system inversion. For stable non-minimum phase systems, an approximation is made leading to an approximate inverse system which is stable. Section IV provides simulation and experimental results on tracking control using the proposed method for a belt-driven H-frame XY positioning system. Conclusions are given in Section V.

5.2 2-DOF Tracking System

In order to use the MIMO inversion algorithm derived in Section III, it is first necessary to design a feedback control system to achieve a desired bandwidth with good stability robustness. As this is not a trivial task, we review in this section a specific methodology for obtaining a 2-degree of freedom (DoF) feedback control system.

Consider an *n*th-order linear, *m*-input, *p*-output plant with state-space model:

$$\begin{aligned} \dot{x} &= Ax + Bu \\ y &= Cx \end{aligned} \tag{5.1}$$

For digital control with sampling interval T seconds we calculate the zero-order hold (ZOH) equivalent plant model

$$\begin{aligned} x[k+1] &= \Phi x + \Gamma u[k] \\ y[k] &= Cx[k] \end{aligned} \tag{5.2}$$

where

$$\Phi = e^{AT} \quad \text{and} \quad \Gamma = \int_0^T e^{AT} B d\tau \tag{5.3}$$

In order to design a control system in which y[k] tracks a class of reference signals r[k] with zero steady-state error, we must use additional dynamics (see Figure 5.1):

$$x_a[k+1] = \Phi_a x_a[k] + \Gamma_a e[k] \tag{5.4}$$

where the eigenvalues of Φ_a are the poles of the z-transform of r[k] [2,3]. For tracking step signals an eigenvalue at $z = 1$ is required, which gives digital integral control. For a MIMO tracking system, the additional dynamics pole(s) must be replicated up to the number of plant outputs. For example, to track step signals for a

plant with p outputs the additional dynamics are given by a parallel combination of p digital integrators:

$$\Phi_a = I_p, \qquad \Gamma_a = I_p \tag{5.5}$$

A digital state-feedback tracking system is shown in Figure 5.1. In order to compute the $m \times n$ state-feedback gain matrix K_1 and the integrator gain matrix K_2, a design model consisting of the cascade of the plant followed by the additional dynamics is needed [3]. This design model is given by:

$$\Phi_d = \begin{bmatrix} A & 0 \\ \Gamma_a C & \Phi_a \end{bmatrix}, \quad \Gamma_d = \begin{bmatrix} \Gamma \\ 0 \end{bmatrix} \tag{5.6}$$

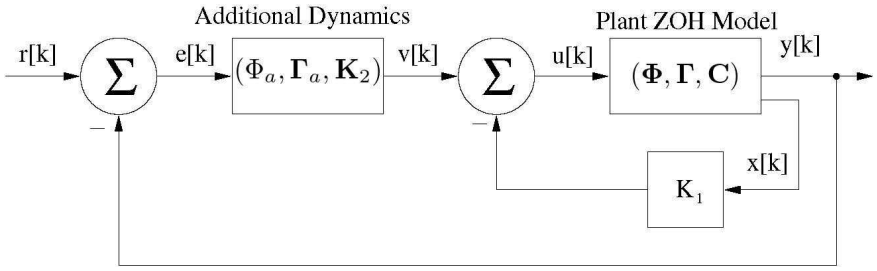

Figure 5.1 A digital State-Space tracking system.

Given a desired set of $n+1$ closed-loop poles, call it zpoles, a $m \times (n+p)$ gain vector K_d is computed to obtain

$$eig(\Phi_d - \Gamma_d K_d) = zpoles. \tag{5.7}$$

Then K_1 consists of the first n columns of K_d and K_2 consists of the last p columns of K_d. In principle, any pole placement algorithm could be used to calculate K_d to achieve (5.7). For a multiple-input plant, however, there are an infinite number of matrices K_d that satisfy (5.7). We recommend a recently developed robust pole-placement

algorithm [4], which uses a parameterization of the set of K_d matrices to find the one which maximizes the input-multiplicative stability robustness bound (see [5] for a definition of this bound).

5.3 Stable MIMO System Inversion

The system shown in Figure 5.1 is a 2 DoF control system having an inner feedback loop around the plant. The model for the system from *v[k]* to *y[k]* will be called the modified plant, and is given as follows:

$$\begin{aligned} x[k+1] &= \Phi_C x[k] + \Gamma v[k] \\ y[k] &= Cx[k] \end{aligned} \tag{5.8}$$

where

$$\Phi_C = \Phi - \Gamma K_1 \tag{5.9}$$

This modified plant is stable due to the feedback through K_1. The transmission zeros of the modified plant might all be inside the unit circle (minimum phase) or some may be outside the unit circle (non-minimum phase). In this subsection we derive a state-space algorithm for inverting a minimum phase system. The following subsection deals with approximately inverting a stable non-minimum phase system. By inverting the modified plant we obtain a feedforward filter that may be used with the control system shown in Figure 5.1 to obtain a precision tracking system.

In order to derive the inverse model for the modified plant (5.8), consider advances of the plant output. Let *r* be the smallest integer for which $C\Phi_C^{r-1}\Gamma$ is a nonzero matrix. Then it can be shown that

$$y[k+1] = C\Phi_C^r x[k] + C\Phi_C^{r-1}\Gamma v[k] \tag{5.10}$$

We assume that the matrix multiplying v[k] is invertible. In some cases it may be necessary to use a different number of advances on each of the plant outputs to get an invertible matrix. The procedure described below may be extended to this case but the details are ommited due to lack of space.

Define

$$D_f = (C\Phi_c^{r-1}\Gamma)^{-1} \tag{5.11}$$

The (5.10) may be rearranged to obtain

$$v[k] = -D_f C\Phi_c^r x[k] + D_f y[k+r]. \tag{5.12}$$

This equation may be substituted into the first equation of (5.8) to obtain

$$\begin{aligned} x[k+1] &= \Phi_f x[k] + \Gamma_f y[k+r] \\ v[k] &= C_f x_c[k] + D_f y[k+r] \end{aligned} \tag{5.13}$$

where D_f is given by (5.12) and

$$\begin{aligned} C_f &= -D_f C\Phi_c^r \\ \Phi_f &= \Phi_c + \Gamma C_f \\ \Gamma_f &= D_f \Gamma \end{aligned} \tag{5.14}$$

Equation (5.13) shows that the system ($\Phi_f, \Gamma_f, C_f, D_f$), which will be called the *inverse modified plant (IMP)*, produces the signal v[k] from the advanced plant output y[k+r], which inverts the modified plant in (5.8) with a delay of r samples. That is, the cascade of the IMP (5.13) and the modified plant (5.8) is a pure delay of *r* samples on each output signal. Thus, the IMP may be used as a feedforward filter in the system in Figure 5.1 to obtain theoretically perfect tracking with a delay of r samples.

The preceding development is useful only if the IMP is stable. The poles of the IMP will include the transmission zeros of the modified plant. If the plant itself is non-

minimum phase, some of the poles of the IMP will be outside the unit circle. Even if the continuous-time plant is minimum phase, some of the eigenvalues of the IMP may be outside the unit circle due to the presence of "sampling zeros." Whatever the cause of unstable eigenvalues of the IMP, additional calculations are needed to obtain a stable approximate inverse for the modified plant, as shown next.

5.3.1 Approximate Inverse for Stable Nonminimum Phase System

Consider adding s more advances to the r advances shown in (5.10). The result is, with d = r + s,

$$y[k+d] = C\Phi_c^d x[k] + \sum_{i=0}^{s} C\Phi_c^{d-i-1} v[k+i]. \tag{5.15}$$

Assume that we are interested in tracking relatively low frequency signals so that v[k] will not change much from sample to sample. We can then make the approximation that

$$v[k+i] \approx v[k], i = 1,...,s \tag{5.16}$$

Substituting this into (5.15) yields

$$y[k+d] \approx C\Phi_c^d x_c[k] + D_f^{-1} v[k] \tag{5.17}$$

Where

$$D_f = \left(\sum_{i=0}^{s} C\Phi_c^{d-i-1}\Gamma \right)^{-1} \tag{5.18}$$

Using the same procedure as before (i.e. solving (5.17) for v[k] and substituting into (5.8)) we obtain an approximate inverse modified plant ($\Phi_f, \Gamma_f, C_f, D_f$) with D_f given by (5.18) and

$$
\begin{aligned}
C_f &= -D_f C \Phi_c^r \\
\Phi_f &= \Phi_c + \Gamma C_f \\
\Gamma_f &= D_f \Gamma
\end{aligned}
\tag{5.19}
$$

The cascade of this IMP with the modified plant will not be a pure delay due to the approximation in (5.16). The frequency range over which the IMP provides an accurate inversion must be evaluated on a case by case basis. However, for sufficiently large d, the IMP will be stable. This is due to the fact that the modified plant is stable, which implies that the eigenvalues of Φ_c are inside the unit circle. The IMP matrix is $\Phi_f = \Phi_c + \Gamma_c C_f$ and the entries of $C_f = -D_f C_c \Phi_c^d$ can be made arbitrarily small by increasing d. Thus, the eigenvalues of Φ_f will move towards the eigenvalues of Φ_c and become stable for sufficiently large d. The value of d is chosen to be the smallest integer greater than r for which the resulting Φ_f has all its eigenvalues inside the unit circle. A precision tracking system is obtained by inserting a feedforward IMP into Figure 5.1 and accounting for the delay of d samples. The result is shown in Figure 5.2.

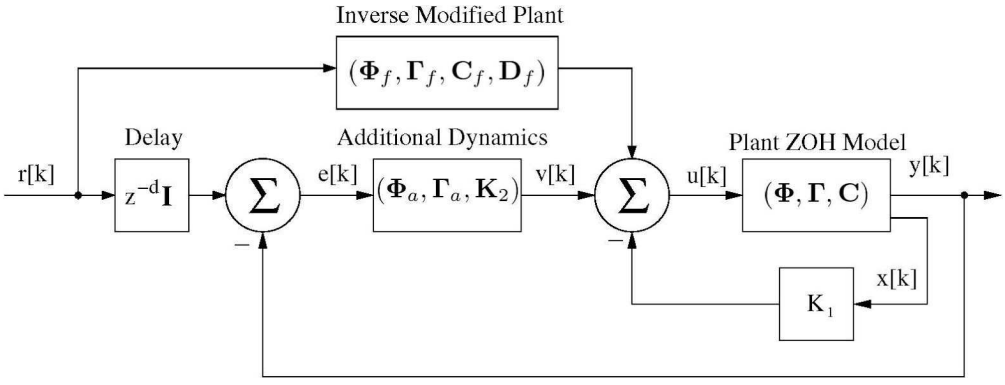

Figure 5.2 A Digital tracking system with inverse Modified Plant (IMP) filter

5.4 Simulation and Experimental Results

In this section we carry out the design and implementation of a tracking control system for an H-Frame XY positioning system. This system consists of two stationary motors, eight pulleys, and a single drive belt, as shown in Figure 5.3. A detailed description of the derivation of an 8th-order state space model is given in [6]. That paper gives the (A, B, C) plant model, and also describes some nonlinear friction in the hardware system. The design methodology and simulation results in this paper do not incorporate the nonlinear friction. It is, of course, present in the hardware results shown in the following subsection. The inputs, outputs, and state variables for this plant are:

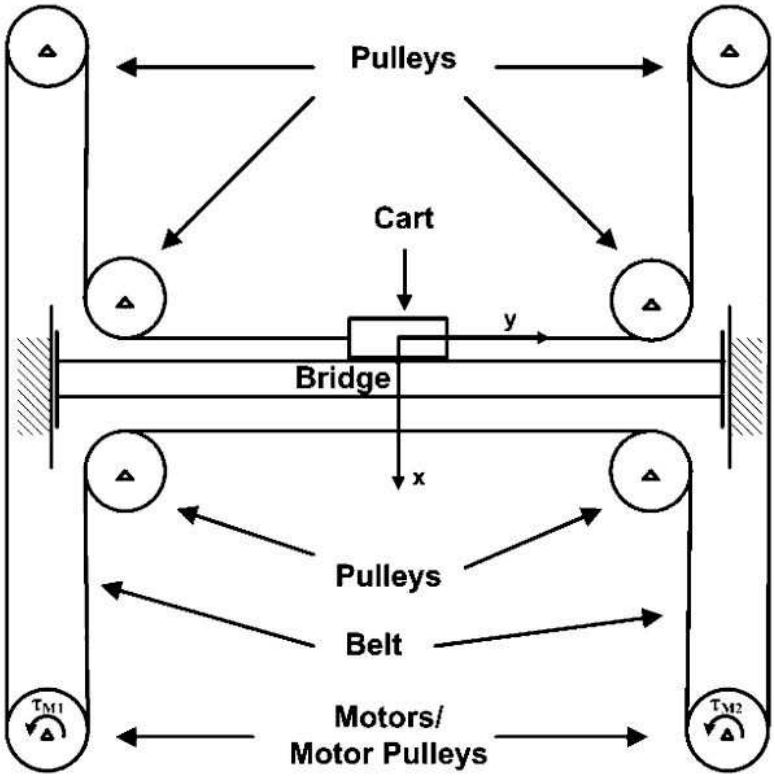

Figure 5.3 An H-frame XY positioning system

x_1 = x postition of cart (m)
x_2 = x velocity of cart (m/s)
x_3 = y postition of cart (m)
x_4 = y velocity of cart (m/s)
x_5 = angular position of motor 1
x_6 = angular velocity of motor 1
x_7 = angular position of motor 2
x_8 = angular velocity of motor 2

The inputs are the voltages to the two motor power amplifiers, and the tracked outputs are the x and y positions of the cart. In order to calculate the gain matrix $K_d = [K_1\ K_2]$ by a pole-placement algorithm, desired closed-loop poles must be selected. This choice is influenced by the locations of the poles and zeros of the continuous-time plant [4,7]. This plant has no finite transmission zeros, and has the following poles:

$$-20 \pm j39, -22 \pm j249, -16, -44, 0, 0. \tag{5.20}$$

Using the rules given in [4] four of the closed-loop poles are selected by keeping the imaginary parts of the complex plant poles and replacing their real parts with a value determined by the desired settling time, call it TS seconds. The value that gives the desired damping is s1/Ts, where s1 is the first order normalized Bessel pole, shown in Table 5.1. For initial simulation results we choose the desired settling time to be

$$T_S = 0.1\text{sec} \tag{5.21}$$

Table 5.1 Normalized Bessel poles for 1st through 6th order systems with 1-second settling time (from [2]). To get a settling time of T_s seconds, divide all poles by T_s.

Variable	Pole Locations
s_1	-4.6200
s_2	$-4.0530 \pm j2.3400$
s_3	$-5.0093, -3.9668 \pm j3.7845$
s_4	$-4.0156 \pm 5.0723, -5.5281 \pm j1.6553$
s_5	$-6.4480, -4.1104 \pm j6.3142, -5.9268 \pm j3.0813$
s_6	$-4.2169 \pm j7.5300, -6.2613 \pm j4.4018, -7.1205 \pm j1.4540$

and the sampling interval was chosen to be T = 0:001 seconds. The design model shown in (5.6) includes the additional dynamics, which are two integrators, giving a 10th order design model. With four of the poles chosen by adding damping to the complex plant poles, the remaining six closed-loop poles are chosen to be s6/Ts (see Table 5.1). With this selection of closed-loop poles, the algorithm described in [4] was used to calculate the gain matrices K_1 and K_2. The input multiplicative stability robustness bound for the resulting tracking system was $\delta = 0.71$. If the gain matrices are calculated using Matlab's place command, the stability robustness bound is 0.36. The robustness bound for state feedback gains computed via an optimal control linear-quadratic regulator (LQR) formulation is guaranteed to be at least 0.5 [5]. The place command gives much less robustness than LQR for this plant, but the new formulation [V] gives robustness that is competitive with LQR with the ease of a pole-placement design. With the gain matrices K_1 and K_2 calculated, the modified plant (5.8) is formed. The poles and zeros of the modified plant are:

$$poles: -0.93 \pm j0.32, 0.95 \pm j24, 0.89 \pm j0.08, 0.93 \pm 0.07$$
$$zeros: -9.69, -9.73, -0.99, -0.98, -0.10, -0.11.$$

This modified plant can be inverted exactly with a delay of r = 1 sample. However, the two zeros outside the unit circle will be unstable poles of the exact inverse model. Furthermore, an exact inverse would have poles at the locations of the zeros of the modified plant on the negative real axis, resulting in a highly oscillatory output signal from the inverse model. Using the procedure described in Section IIB, it is found that only one additional delay, s = 1, is needed to make the IMP stable. With d = r + s = 2 delays, the poles and zeros of the IMP are:

$$poles: -0.27 \pm j0.54, -0.25 \pm j0.57, 0.1434, 0.15, 0, 0.$$
$$zeros: -0.93 \pm j0.32, 0.95 \pm 0.24, 0.89 \pm 0.08, 0.93 \pm 0.07$$

As expected, the zeros of the IMP are the poles of the modified plant. However, looking at the poles of the IMP, it is not clear how they are approximating the unstable and negative-real axis zeros of the modified plant. Nevertheless, the IMP produces an inverse of the plant that is a very good approximation from 0 to about 80 Hz. This might be expected because only one additional delay was need, and with s = 1, the approximation in (5.16) will be very good. Figure 5.4 shows a simulation result in which the reference trajectory causes the cart to move along a square whose sides have length 2.5 cm. The x and y positions of the cart are equal to the reference trajectories, which have been delayed by two samples. This plot shows that the IMP provides theoretically perfect tracking for this reference signal. The same reference signal was used with the hardware H-frame system and the results are shown in Figure 5.5. In the hardware system, the tracking errors were smaller than $5 \times 10^{-4} m$.

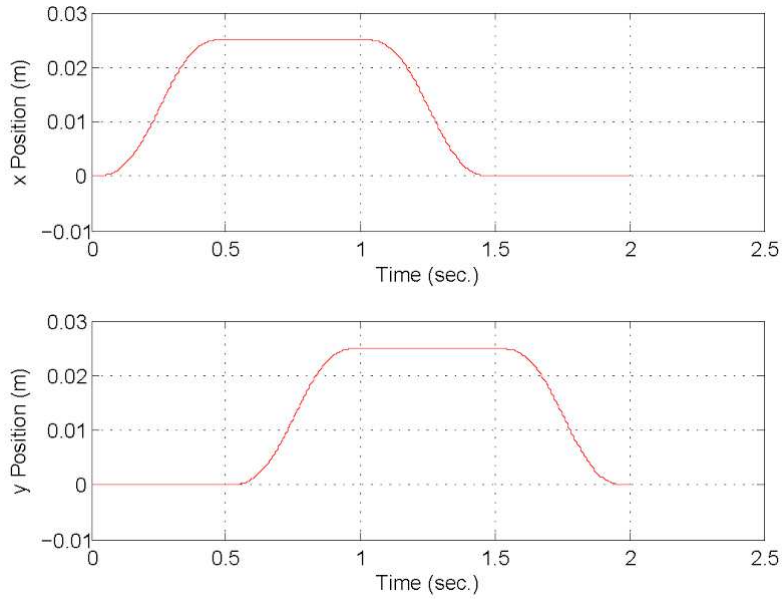

Figure 5.4 Simulated x and y reference and achieved trajectories for tracking system shown in Figure 5.2.

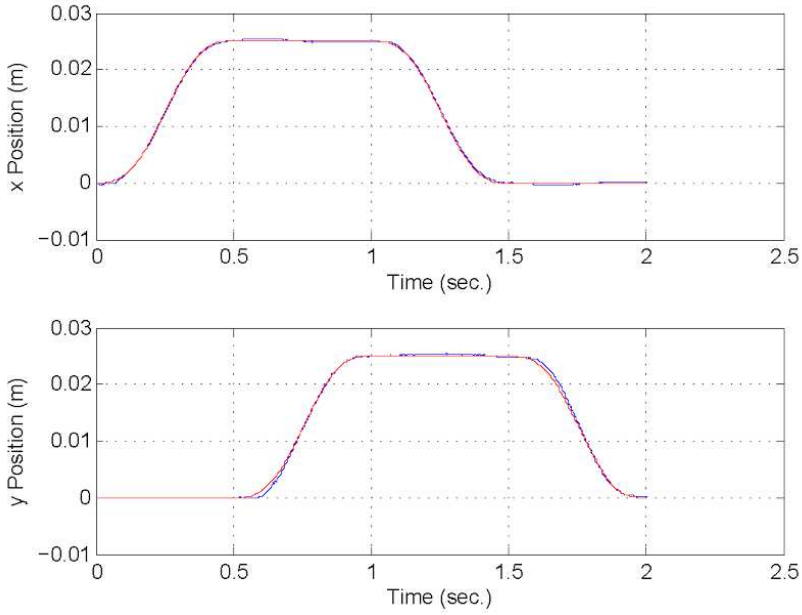

Figure 5.5 Experimental x and y reference (red) and achieved (blue) trajectories for the H-frame system using the tracking system shown in Figure 5.2. The tracking errors are less than $5\times10^{-4}\,m$.

In order to show the effect of the IMP on the tracking performance, the IMP was disconnected and the tracking system of Figure 5.2 was implemented on the hardware system. The results are shown in Figure 5.6. There is significant delay and distortion in the cart trajectory. These are effectively removed by the IMP, as seen in the previous figure.

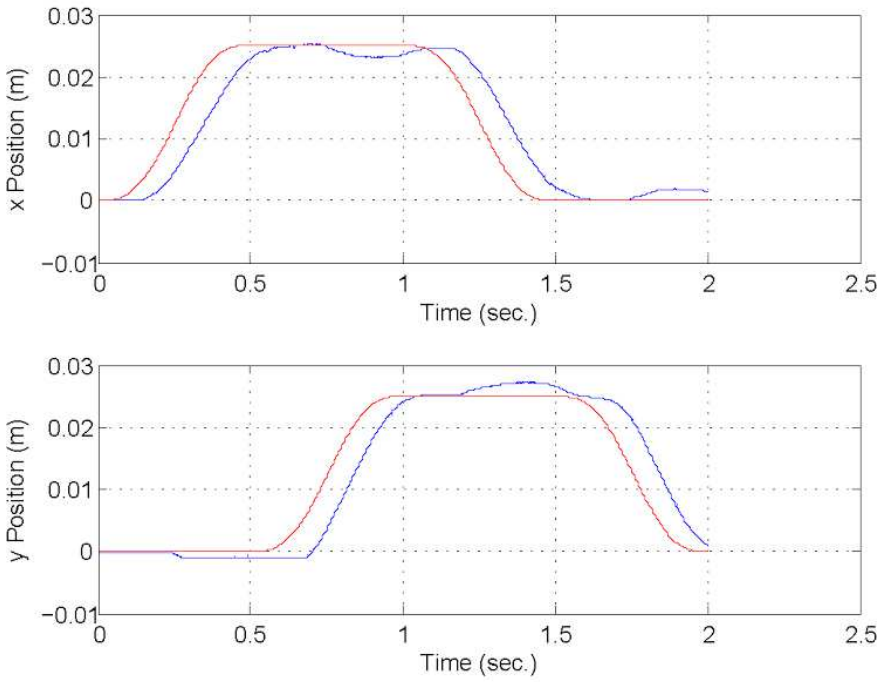

Figure 5.6 Experimental x and y reference (red) and achieved (blue) trajectories for the H-frame system using the tracking system shown in Figure 5.2 without the Inverse Modified Plant filter.

5.5 Conclusion

A method of obtaining an approximate inverse of a non-minimum phase MIMO system was presented and confirmed with simulations and experimental results. The example used a relatively low frequency reference signal. In the hardware system, attempts at higher speed trajectories resulting in chattering, which is thought to be caused by the nonlinear friction that is present. The proposed control techniques used in this paper are for linear systems. A friction-compensation scheme such as shown in [8] might be used to make the hardware system behave more like a linear system, allowing higher tracking speeds.

References

[1] M. Heertjes and D. Bruijnen, "MIMO FIR Feedforward Design for Zero Error Tracking Control," in Proceeding 2014 American Control Conference, pp. 2166–2171, Portland, OR, USA, June 4-6, 2014.

[2] E.J. Davison and A. Goldenberg, "Robust Control of a General Servomechanism Problem: the Servo Compensator," Automatica, vol. 11, pp. 461—471, 1975.

[3] R.J. Vaccaro, Digital Control: A State-Space Approach, McGraw-Hill, New York, NY; 1995.

[4] R.J. Vaccaro, "An Optimization Approach to the Pole-Placement Design of Robust Linear Multivariable Control Systems," in Proceeding 2014 American Control Conference, pp. 4298–4305, Portland, OR, USA, June 4-6, 2014.

[5] J.B. Burl, Linear Optimal Control, Addison Wesley Longman, Menlo Park, CA, 1999.

[6] K.S. Sollmann, M.K. Jouaneh, and D. Lavender, "Dynamic Modeling of a Two-Axis, Parallel, H-Frame-Type XY Positioning System," IEEE/ASME Trans. Mechatronics, vol. 15, no. 2, pp. 280–290, April, 2010.

[7] K.J. Astrom and R.M. Murray, Feedback Systems, pg. 362, Princeton University Press, Princeton, NJ, 2008.

[8] R.J. Vaccaro, "Friction Compensation Without a Friction Model," in Proc. 2012 American Control Conf., pp. 4739–4744, Montreal, Canada, June 27